Combining Discrete Equations Method and upwind downwind-controlled splitting for non-reacting and reacting two-fluid computations

Kunkun Tang, Alberto Beccantini, Christophe Eric Corre

Seventh International Conference on Computational Fluid Dynamics (ICCFD7), Big Island, Hawaii, July 9-13, 2012

ICCFD7-3003

Combining Discrete Equations Method and upwind downwind-controlled splitting for non-reacting and reacting two-fluid computations

Kunkun Tang*, Alberto Beccantini* and Christophe Corre**
Corresponding author: kunkun.tang@cea.fr, alberto.beccantini@cea.fr

* CEA Saclay, Lab. for Applications in Thermal Hydraulics and Fluid Mechanics, DEN/DM2S/STMF, 91191 Gif-sur-Yvette Cedex, France.
** Grenoble-INP/UJF Grenoble/CNRS LEGI UMR5519, Domaine Universitaire BP 53, 38041 Grenoble, France.

Abstract: The reactive Riemann solver proposed in [1] is inserted into the Reactive Discrete Equations Method (RDEM) [2, 3] to compute high speed combustion waves. The anti-diffusive approach developed in [4] is also coupled with RDEM to accurately simulate reacting shocks [5]. Increased robustness and efficiency when computing both multiphase interfaces and reacting flows are achieved thanks to an original upwind downwind-controlled splitting method (UDCS).

Keywords: interface, two-fluid model, nonconservative systems, compressible multifluid flows, (Reactive) Discrete Equations Method, reacting interface, deflagration, detonation, anti-diffusive scheme, upwind downwind-controlled splitting

1 Introduction

The use of Computational Fluids Dynamics (CFD) for industrial applications often implies the capability of dealing with geometries which are large with respect to the characteristic dimensions of the involved physical phenomena. Such situations arise for instance when computing the pressure loads generated by a hydrogen-air combustion occurring in a nuclear reactor containment during a postulated Loss of Coolant Accident. The free volume of the European Pressurized Reactor building is about 75000 m^3 while the characteristic physical lengths of the combustion flame are much smaller: the reaction zone in a laminar deflagration at atmospheric condition can vary from about 1 mm to 10 mm; consequently, the "direct simulation" of flame propagation and deflagration-to-detonation transition (DDT) in such a large-scale geometry requires prohibitively large mesh sizes. Alternatively, the direct simulation can be avoided by considering the flame as infinitely thin and by modeling the diffusion effects through phenomenological laws for the flame speed. The combustion-induced pressure loads can then be correctly predicted provided the flame speed is correctly estimated. In [6], a combustion algorithm called CREBCOM is proposed to study fast deflagrations and detonations in large geometries. In this algorithm the species diffusion and the thermal diffusivity are neglected and replaced by the introduction of a burning rate constant, which has the dimensions of a speed and plays the same role as the fundamental flame speed. The CREBCOM algorithm is very simple to implement in a CFD code, which resolves the non-reactive Euler equations: the reactive contribution is added by simply introducing a source term. It has been successfully implemented in several industrial purpose CFD codes, such as TONUS [7], to investigate turbulent combustion flows. The main drawback of the CREBCOM algorithm is that it involves a binary criterion function that specifies whether the control volume is burnt or not. Numerical experiments [8] have shown this criterion function can create numerical oscillations in the pressure which strongly affect the flow when the flame speed is low with respect to the sound speed (low Mach number regime). When looking for a combustion model which keeps the simplicity of CREBCOM (no flame surface reconstruction)

while not involving combustion criterion, the Reactive Discrete Equations Method (RDEM) appears as an attractive strategy. Initially proposed in [3] to model evaporation fronts, the RDEM method extends to the reactive Euler equations the Discrete Equations Method (DEM) introduced in [2] for two-phase mixtures and interface problems. The DEM approach consists in the integration of interface problems solutions over a two-phase control volume where the solutions are provided by Riemann solvers. DEM has been initially developed to study multiphase mixtures in which the global averaging of a variable in a control cell would lead to unacceptable numerical errors. The RDEM approach displays several interesting features for computing combustion problems: it does not involve flame surface reconstruction and can be used both for deflagration and denotation; it is also conservative, which means that total mass and energy are conserved in a closed and isolated system (this property is fundamental when computing the combustion in large geometry if the AICC state is to be recovered at the end of the combustion process). The price to pay however is the need to solve a reactive Riemann problem between the burnt and unburnt regions. Such a reactive Riemann solver has been proposed in [1] for thermally perfect gases and used to design an "all shock" approximate Riemann solver which is eventually combined with the RDEM approach to successfully compute high speed deflagrations and denotations. Keeping in mind the large scale of the geometry in the targeted applications, the use of rather coarse meshes is hardly avoidable. As expected, the numerical results obtained in [1] with a first order version of the RDEM approach do not yield a sufficient accuracy of the flame profile, especially for fast deflagration and denotation configuration. Following the initial proposal made in [2], a second order (limited) MUSCL approach could be used. As a further accuracy improvement, the downwind-controlled (anti-diffusive) reconstruction method recently proposed in [4, 9] was coupled with the RDEM approach and compared with the conventional second order MUSCL reconstruction approach. The downwind-controlled method coupled with the RDEM approach was found to be very accurate for computing detonation fronts but unstable for deflagration fronts [5]. In order to better understand the coupling between the RDEM approach and the downwind-controlled method for combustion simulation, it was decided to investigate impermeable interface problems (non-reacting flows) using DEM and the downwind-controlled method. The computation of gas-liquid flows, where each phase is described by the stiffened gas equation of state, led to the development of an original upwind downwind-controlled splitting (UDCS) method with attractive accuracy and robustness properties when coupled with the DEM approach; this UDCS strategy was also successfully inserted into RDEM. The improvement brought by the present work with respect to [9] where an anti-diffusive numerical scheme is introduced for the simulation of interfaces between compressible fluids lies in the capacity of the newly developed method to solve non-reacting and reacting flows, including flame fronts at all combustion regimes, on general multi-dimensional unstructured meshes.
The present paper is devoted to the description of this newly developed numerical strategy, both for non-reacting and reacting flows, and is organized as follows: Section 2 briefly reviews the physical modeling ingredients involved in the study, such as the local and averaged conservation laws governing the evolution of each phase (liquid/gas for non-reacting flows, unburnt/burnt mixture phase for reacting flows), the equations of state and the phase characteristic function; Section 3 describes the (Reactive) Discrete Equations Method applied to the two-phase model; Section 4 introduces the proposed upwind downwind-controlled splitting for an accurate and robust computation of the interface. Numerical results obtained by combining DEM/RDEM with UDCS are displayed and analyzed in Section 5. Conclusions are eventually drawn and some perspectives are outlined. Technical details regarding the mathematical description of the upwind downwind-controlled splitting in multiple space dimensions are reported in Appendix A.

2 Physical model

2.1 Local conservation equations inside each phase

In view of the two-phase flow involved in our applications, the two-fluid model [10, 11] is particularly interesting, which considers each phase separately and thus includes two sets of conservation equations. Neglecting the body force, the fluid viscosity and any heat transfer phenomena, the exact equations of motion, valid inside phase Σ_k, are the Euler equations of gas dynamics:

$$
\begin{aligned}
&\frac{\partial \rho_k}{\partial t} + \nabla \cdot \rho_k \mathbf{v}_k = 0, \\
&\frac{\partial \rho_k \mathbf{v}_k}{\partial t} + \nabla \cdot \Big(\rho_k \mathbf{v}_k \otimes \mathbf{v}_k + p_k \mathbf{I} \Big) = 0, \\
&\frac{\partial}{\partial t} \rho_k \Big(\tilde{e}_k + \frac{1}{2} |\mathbf{v}_k|^2 \Big) + \nabla \cdot \left[\rho \mathbf{v}_k \Big(\tilde{e}_k + \frac{1}{2} |\mathbf{v}_k|^2 \Big) + p_k \mathbf{v}_k \right] = 0,
\end{aligned}
\tag{1}
$$

where ρ is the density, $\mathbf{v}$ is the vector of velocity, p is the pressure, $\tilde{e}$ is the internal energy containing the sensible energy e and the enthalpy of formation h_0 useful in case of reactions.

2.2 Equations of state

The reacting or non-reacting flow problem here considered is described by the two-fluid model which involves two phases with their own thermodynamic variables. A physical mixture is not involved in the modeling of the interface problems considered in this study, but a numerical mixture is unavoidable from a numerical viewpoint. However, as will be detailed in Section 3, it is not necessary to define the mixture EOS within the numerical mixture when using the two-fluid model along with the Discrete Equations Method (DEM). Thus, the EOS involved in present work are only related to each single phase.

2.2.1 Non-reacting case

A popular EOS for describing in a unified way a liquid and a gaseous phase is the stiffened gas EOS [12]:

$$
p_k = (\gamma_k - 1)\rho_k(\tilde{e}_k - h_{0,k}) - \gamma_k p_{\infty,k}, \tag{2}
$$

where the enthalpy of formation h_0 can be set to zero for applications dealing with impermeable interfaces, since no such energy, due to the reaction process or phase change, is released. The constant coefficients $\gamma,\ p_\infty$ are set to $\gamma = 4.4$ and $p_\infty = 6 \times 10^8$ for water. The gases considered in the study of non-reacting interfaces are governed by the polytropic gas EOS with $p_\infty = 0$ in (2) (see [13] for further investigation of stiffened gases). Note that negative pressure p can arise for liquids in the stiffened gas model (2) when strong rarefaction waves occur, which can create numerical difficulties. No specific treatment concerning negative pressure is done in this work since system (1) remains hyperbolic and mathematically well-posed as long as the square of sound speed $c^2 = \frac{\gamma(p+p_\infty)}{\rho}$ remains positive. Alternatively, [3] proposes an evaporation solver for (2) in which liquid is transformed into vapor or liquid-vapor mixture when its pressure is inferior to the saturated one.

2.2.2 Reacting case

The EOS of thermally perfect gases is used to describe the unburnt and burnt gas mixtures [1]:

$$
\begin{aligned}
p_k &= \rho_k \mathscr{R}_k T_k, \\
\tilde{e}_k &= h_{0,k} + \int_0^{T_k} c_{v,k}(\tau)\, \mathrm{d}\tau,
\end{aligned}
$$

where $\mathscr{R}$ is the gas constant, T is the temperature, and $c_v(T)$ is the specific heat at constant volume which depends on the temperature. In the reaction problem, the enthalpy of formation of the unburnt gas is released and transformed into the heat of reaction and the sensible energy of the burnt gas.

2.3 Phase characteristic function X_k

When simulating the interface evolution between two phases, it is useful to determine the position of the interface. In [14], the *characteristic function* $X_k(\mathbf{x}, t; \Sigma_k)$ of phase Σ_k is defined to this purpose:

$$
X_k(\mathbf{x}, t; \Sigma_k) = \begin{cases} 1, \text{ if } \mathbf{x} \text{ lies in phase } \Sigma_k \text{ at } t; \\ 0, \text{ otherwise.} \end{cases}
$$

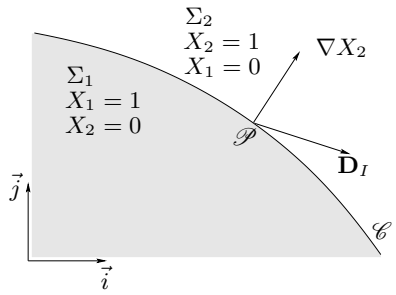

Figure 1: Characteristic function X. The phase Σ_1 is shaded, and characterized by $X_1 = 1$ whereas the phase Σ_2 is in white, and characterized by $X_2 = 1$. The interface between the phases is represented by the curve $\mathscr{C}$, and D_I is its velocity at point $\mathscr{P}$. ∇X_1 and ∇X_2 are both perpendicular to the interface curve $\mathscr{C}$ at $\mathscr{P}$.

The function X_k (see Fig. 1) indicates the phase Σ_k and ignores all other phases and interfaces. The interface is thus characterized by the discontinuity of the characteristic function X_k. According to [14], the *topological equation* for X_k follows,

$$\frac{\partial X_k}{\partial t} + \mathbf{D}_I \cdot \nabla X_k = 0, \tag{3}$$

where $\mathbf{D}_I$ is the propagation velocity of the non-reacting or reacting interface. Since (3) means the material derivative of X_k following the interface vanishes, this topological equation describes the geometrical evolution of the interface.

2.4 The averaged equations of two-fluid model for interfaces

Applying an averaging procedure (not detailed here) to the Euler equations (1) and the characteristic function equation yields the two-fluid model for a two-phase flow [10, 11], which includes mass, momentum and energy conservation equations (4), (5), and (6) for each phase Σ_k involved in the interface propagation.

Mass

$$\frac{\partial \alpha_k \rho_k}{\partial t} + \nabla \cdot \alpha_k \rho_k \mathbf{v}_k = \rho_{k,I}\Big(\mathbf{v}_{k,I} - \mathbf{D}_I\Big) \cdot \nabla \alpha_k; \tag{4}$$

Momentum

$$\frac{\partial \alpha_k \rho_k \mathbf{v}_k}{\partial t} + \nabla \cdot \alpha_k \Big(\rho_k \mathbf{v}_k \otimes \mathbf{v}_k + p_k \mathbf{I}\Big) = \Big[\rho_{k,I} \mathbf{v}_{k,I} \otimes \Big(\mathbf{v}_{k,I} - \mathbf{D}_I\Big) + p_{k,I}\mathbf{I}\Big] \cdot \nabla \alpha_k; \tag{5}$$

Energy

$$\begin{aligned} &\frac{\partial}{\partial t} \alpha_k \rho_k \Big(\tilde{e}_k + \frac{1}{2}|\mathbf{v}_k|^2\Big) + \nabla \cdot \alpha_k \Big[\rho_k \mathbf{v}_k \Big(\tilde{e}_k + \frac{1}{2}|\mathbf{v}_k|^2\Big) + p_k \mathbf{v}_k\Big] \\ &\quad = \Big[\rho_{k,I}\Big(\tilde{e}_{k,I} + \frac{1}{2}|\mathbf{v}_{k,I}|^2\Big)\Big(\mathbf{v}_{k,I} - \mathbf{D}_I\Big) + p_{k,I}\mathbf{v}_{k,I}\Big] \cdot \nabla \alpha_k. \end{aligned} \tag{6}$$

The variable α_k appearing in this two-fluid model is the averaged value of characteristic function X_k, and is often called the *volume fraction*. The above governing equations involve non-conservative phase interaction terms. It will be seen in the next Section how the DEM/RDEM approach allows to overcome the difficult task of physically modeling the interface variables. The system is coupled with the averaged transport equation (7) derived from the topological equation (3):

Volume fraction

$$\frac{\partial \alpha_k}{\partial t} + \mathbf{D}_I \cdot \nabla \alpha_k = 0, \tag{7}$$

The variables involved in the interface problem to solve are the volume fraction α_k of phase Σ_k, and its corresponding averaged phase variables $\alpha_k \mathbf{u}_k$, where $\mathbf{u}$ is the vector of average conservative variables representing the mass, momentum, and total energy in the one-phase system (1).

3 (Reactive) Discrete Equations Method for two-fluid model

3.1 General principles

The (Reactive) Discrete Equations Method (DEM/RDEM) [2, 3] is retained in this work to deal with the reacting and non-reacting interfaces. The description provided here is focused on operational issues (how to implement DEM/RDEM); see [2, 3] for more detailed explanations. The DEM/RDEM used in the present work is an Eulerian approach (fixed space grid); an extension of DEM/RDEM to the Arbitrary Lagrangian-Eulerian approach (ALE) can be found in [15, 16].
The two-phase flow here considered is characterized by the volume fraction of each phase. Even though only the interfaces (permeable or impermeable) separating the pure fluids should be involved in the problem, non-zero volume fractions must be defined at each location to preserve the hyperbolicity of the two-fluid model with two pressures and two velocities [17, 18]. Due to numerical dissipation, the volume fraction at the interface is diffused, which artificially creates numerical mixture. In Fig. 2, the diffused volume fractions illustrate the numerical mixture of material interface in one space dimension.
As in the Godunov's scheme for the single phase compressible Euler equations, local Riemann problems are considered in the DEM/RDEM method for the averaging of conservative variables, or more practically for the intercell numerical flux functions. At each cell boundary in the interface diffusion zone for the volume fraction model in Fig. 3, the unitary surface can be divided into three parts, depending upon the phase configuration across the intercell boundary. This intercell boundary partition results in three different local Riemann problems at each intercell location, for instance at the position $x_{i-\frac{1}{2}}$ in case that $\alpha_{1,i-1} > \alpha_{1,i}$ (and $\alpha_{2,i-1} < \alpha_{2,i}$): RP11$\big(\mathbf{U}^n_{1,i-1}, \mathbf{U}^n_{1,i}\big)$, RP12$\big(\mathbf{U}^n_{1,i-1}, \mathbf{U}^n_{2,i}\big)$, and RP22$\big(\mathbf{U}^n_{2,i-1}, \mathbf{U}^n_{2,i}\big)$. Let us emphasize that, with the DEM/RDEM approach, the Riemann problem RP21$\big(\mathbf{U}^n_{2,i-1}, \mathbf{U}^n_{1,i}\big)$ is not taken into account in the specific case shown in Fig. 3. Firstly, from a physical viewpoint, the interface considered in the present work can not involve RP12 and RP21 at the same time and the same location. Secondly, from a numerical viewpoint, when the two phases are separated in the two-phase control volumes (as in Fig. 3 in DEM/RDEM approach for $\alpha_{1,i-1} > \alpha_{1,i}$), there is no such contact surface at the intercell boundary $x_{i-\frac{1}{2}}$ which has phase Σ_2 as left state and phase Σ_1 as right state.
As far as the one-phase local Riemann problems RP11 and RP22 are concerned, the conventional Godunov flux for the Euler equations (1) $\mathbf{F}^{\mathrm{GOD}}(\mathbf{U}^{(11)}_{i-\frac{1}{2}})$ and $\mathbf{F}^{\mathrm{GOD}}(\mathbf{U}^{(22)}_{i-\frac{1}{2}})$ ([19] for stiffened gases, [1] for thermally perfect gases) can be used for the updating of the phase variables. Alternatively, any suitable approximate

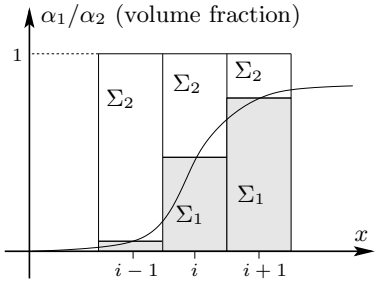

Figure 2: Numerically diffused volume fractions. The phase Σ_1 is shaded, and characterized by the volume fraction α_1 whereas the phase Σ_2 is in white, and characterized by α_2. $\alpha_1 + \alpha_2 = 1$.

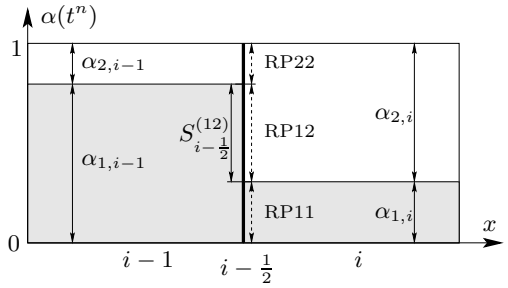

Figure 3: Three Riemann problems at the intercell boundary $i-\frac{1}{2}$. The phase Σ_1 is shaded whereas the phase Σ_2 is in white.

Riemann solver [20] can be employed for RP11 and RP22.
The two-phase local Riemann problem RP12 requires a specific treatment for the discretization of the non-conservative transport equation for volume fractions (7) and the updating of the corresponding phase variables. The two-phase Riemann problem structure for non-reacting stiffened gas is presented in Section 3.2, and that of reacting thermally perfect gases is described in Section 3.3. The treatment for the two-phase local Riemann problem RP12 depends on whether the interface velocity D_I is positive or negative. If $D_I > 0$, the phase Σ_1 enters into the cell i with the velocity D_I; otherwise, the phase Σ_2 enters into the cell $i-1$ with the velocity D_I. In the following description, focused on cell i, D_I is supposed to be positive at $x_{i-\frac{1}{2}}$ and $x_{i+\frac{1}{2}}$ with $\alpha_{1,i-1} > \alpha_{1,i} > \alpha_{1,i+1}$. The situation of overall two-phase control volumes at time $t^{n+1} = t^n + \Delta t$ is sketched in Fig. 4. The two-phase interface (Σ_1, Σ_2) represented by BC at $x_{i-\frac{1}{2}}$ at time t^n moves to the right with velocity D_I and reaches position $B'C'$ ($x = x_{i-\frac{1}{2}} + D_I\Delta t$) at t^{n+1}. The sub-volume of $BCC'B'$ initially occupied by phase Σ_2 (Fig. 3) is now occupied by Σ_1 (Fig. 4). Thus, the variations of phase volume fraction in cell element i can be quantified as:

$$\begin{aligned} \Delta\alpha^n_{1,i} &= S^{(12)}_{i-\frac{1}{2}} \frac{D_I \Delta t}{\Delta x}; \\ \Delta\alpha^n_{2,i} &= -S^{(12)}_{i-\frac{1}{2}} \frac{D_I \Delta t}{\Delta x}, \end{aligned} \tag{8}$$

where $S^{(12)}_{i-\frac{1}{2}}$ denotes the surface of Riemann problem RP12 at the intercell boundary $x_{i-\frac{1}{2}}$ (see Fig. 3) and can be defined as:

$$S^{(12)}_{i-\frac{1}{2}} \overset{\text{def}}{=} \max\Big\{0, \alpha_{1,i-1} - \alpha_{1,i}\Big\} \overset{\text{or}}{=} \max\Big\{0, \alpha_{2,i} - \alpha_{2,i-1}\Big\}.$$

Indeed, the formulation (8) corresponds to the discretization of the volume fraction equation (7), which can be interpreted by the volume $BCC'B'$ in Fig. 4. To explain the averaging procedure of phase variables in the DEM/RDEM approach, the Riemann problems for surface segment BC at location $x_{i-\frac{1}{2}}$ and for DE at location $x_{i+\frac{1}{2}}$ are illustrated in Fig. 5 in the case of non-reacting stiffened gas flows, where the interface

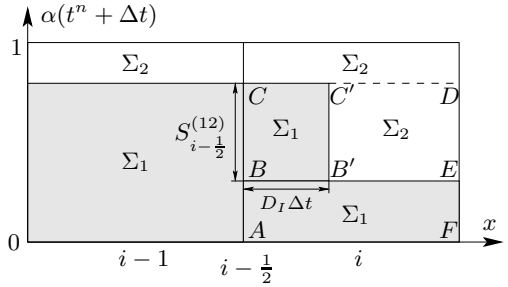

Figure 4: Two-phase control volumes at time $t^n + \Delta t$. The interface represented by BC at $x_{i-\frac{1}{2}}$ at time t^n moves to the right with the velocity of D_I and arrives at position $B'C'$ ($x = x_{i-\frac{1}{2}} + D_I\Delta t$) at $t^{n+1} = t^n + \Delta t$.

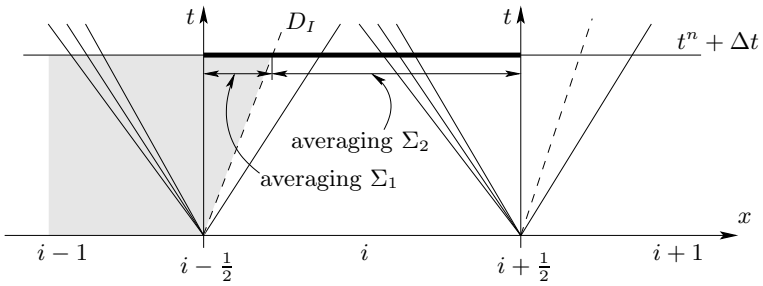

Figure 5: Two-phase local Riemann problem RP12 at intercell position $x_{i-\frac{1}{2}}$ linked to the surface segment BC in Fig. 4, and the corresponding one-phase local Riemann problem RP22 at intercell position $x_{i+\frac{1}{2}}$ linked to the surface segment DE in Fig. 4. At t^n, the sub-volume $BCDE$ of element i (Fig. 4) is entirely occupied by the phase Σ_2 (in white). D_I corresponds to the interface velocity. At t^{n+1}, one part of $[x_{i-\frac{1}{2}}, x_{i-\frac{1}{2}} + D_I\Delta t]$ in the sub-volume $BCDE$ is occupied by the phase Σ_1 (shaded). So Σ_1 is averaged aver $[x_{i-\frac{1}{2}}, x_{i-\frac{1}{2}} + D_I\Delta t] \times t^{n+1}$, and Σ_2 is averaged aver $[x_{i-\frac{1}{2}} + D_I\Delta t, x_{i+\frac{1}{2}}] \times t^{n+1}$.

velocity D_I is equal to the velocity of contact discontinuity. It is worthwhile to notice that in order to perform the variables averaging for both phases in DEM/RDEM method, it is first needed to assume that no wave interaction occurs within computational cells. This is satisfied by the CFL restriction of CFL $\leq \frac{1}{2}$. Thus, the averaging of conservative variables for each phase concerning the sub-cell $BCDE$ in Fig. 4 inside the element i can be expressed, by integrating over the line segment $[x_{i-\frac{1}{2}}, x_{i+\frac{1}{2}}] \times t^{n+1}$ in Fig. 5, as

$$\mathbf{U}_{1,i}^{n+1}\big|_{BCC'B'} = \int_{x_{i-\frac{1}{2}}}^{x_{i-\frac{1}{2}}+D_I\Delta t} \mathbf{U}_{i-\frac{1}{2}}^{(12)}\left(x, t^{n+1}\right) \mathrm{d}x,$$

$$\mathbf{U}_{2,i}^{n+1}\big|_{B'C'DE} = \int_{x_{i-\frac{1}{2}}+D_I\Delta t}^{x_{i-\frac{1}{2}}+\frac{1}{2}\Delta x} \mathbf{U}_{i-\frac{1}{2}}^{(12)}\left(x, t^{n+1}\right) \mathrm{d}x + \int_{x_{i+\frac{1}{2}}-\frac{1}{2}\Delta x}^{x_{i+\frac{1}{2}}} \mathbf{U}_{i+\frac{1}{2}}^{(22)}\left(x, t^{n+1}\right) \mathrm{d}x,$$

where $\mathbf{U}_{i-\frac{1}{2}}^{(12)}$ is the solution of local Riemann problem RP12 at $x_{i-\frac{1}{2}}$, and $\mathbf{U}_{i+\frac{1}{2}}^{(22)}$ is the solution of local Riemann problem RP22 at $x_{i+\frac{1}{2}}$ (surface area DE in Fig. 4 is covered by RP22 at $x_{i+\frac{1}{2}}$). The conservative variables in the volume $ABEF$ in Fig. 4 for phase Σ_1 are updated by the conventional Godunov's flux (or with approximated solver) at the surface areas AB and EF. Concluding for the cell element i, the volumes $BCC'B'$ and $ABEF$ in Fig. 4 are responsible for the averaging of conservative variables for the phase Σ_1, and in the same manner, the remaining volume inside cell i is linked to the averaging for the phase Σ_2. In other words, the averaging of conservative variables is realized separately for the two phases, which, consequently, also avoids averaging the thermodynamic properties. This characteristic property of the DEM/RDEM method prevents the occurrence of non-physical pressure oscillations at the material interface [21].

However, it is difficult to handle the averaging of conservative variables, when a more efficient time-marching scheme is required. Indeed, due to the non-linear wave interactions in case of CFL $> \frac{1}{2}$, the determination of phase variables at the next time step is no longer obvious. On the other hand, as for the conservative form of the Godunov's method, the DEM/RDEM method can be written in terms of numerical flux for practical computations (see [2, 3]). Since a moving interface is involved in the two-phase Riemann problem RP12, a so-called Lagrangian flux is required. It can be understood as a flux function across a moving boundary of the corresponding phase, representing the phase interactions. By applying the DEM/RDEM method with the numerical flux for two-phase Riemann problems (Eulerian one and Lagrangian one), the CFL restriction of CFL $\leq \frac{1}{2}$ can be extended to CFL ≤ 1, provided that no wave acceleration takes place as a consequence of wave interaction [20]. Note however that, within the framework of DEM/RDEM approach, additional restriction for time step Δt must be respected for the volume fraction (see condition (17)).

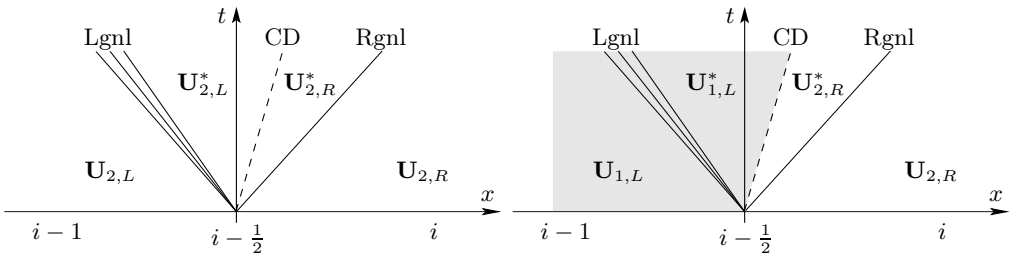

(a) RP22 (b) RP12

Figure 6: Local Riemann problems in case of non-reacting stiffened gas flows at intercell position $x_{i-\frac{1}{2}}$. (a) is the solution structure of one-phase Riemann problem RP22($\mathbf{U}^n_{2,i-1}, \mathbf{U}^n_{2,i}$) which contains a left genuinely non-linear wave (Lgnl), a contact discontinuity (CD), and a right genuinely non-linear wave (Rgnl); (b) is the two-phase Riemann problem RP12($\mathbf{U}^n_{1,i-1}, \mathbf{U}^n_{2,i}$) with the same structure as the one-phase problem (a). The velocity of the contact discontinuity in (b) is the interface velocity D_I.

3.2 Local Riemann problem in non-reacting case

The solution of the local Riemann problem is the essential ingredient in numerical methods for compressible flows. For the stiffened gas problem in the non-reacting case within the DEM approach, any suitable approximated Riemann solver [20, 19] can be used to evaluate the numerical flux. The numerical results presented in this work are obtained with the exact Riemann solver [19]. The one-phase local Riemann problems RP11 and RP22 have the same solution structure as the two-phase ones RP12 or RP21. For instance, the typical solutions of RP22 and RP12 are illustrated in Fig. 6. The velocity of contact discontinuity v^* in the two-phase Riemann problem (e.g. Fig. 6(b)) is inserted into the volume fraction transport equation (7) as the average interface velocity D_I in one space dimension. On the other hand, the pressure p^* inside the star region in the two-phase Riemann problem is set as the interface pressure p_I when calculating the moving flux (Lagrangian flux) across the interface. Consequently, the difficult physical modeling for interface conditions (D_I and p_I) in two-phase flow is avoided by using numerical data [22, 2].
Regarding the general multi-dimensional case, rotational invariance is valid for the governing equations of two-fluid model (4)-(7). Thus, one-dimensional Riemann problem can be used for computing the multi-dimensional numerical flux. At each intercell boundary of a general mesh, the solution of a local one-dimensional two-phase Riemann problem gives the propagation speed of the volume fraction in the normal direction of the intercell boundary. This kind of approximation reflects the averaged interface velocity $\mathbf{D}_I$ in transport equation (7) within the framework of DEM/RDEM approach.

3.3 Local Riemann problem in reacting case

The reacting interface problem also involves the local Riemann problems RP11, RP22, and RP12 or RP21 within the RDEM approach. As far as the one-phase non-reacting problems (RP11, RP22) are concerned, any approximated Riemann solver [20] or exact Riemann solver [23] can be applied for thermally perfect gases with temperature-dependent specific heats. The exact wave structure of RP11 or RP22 is similar to the one of non-reacting stiffened gas (Fig. 6(a)). The wave structure of the two-phase reactive Riemann problem RP12 or RP21 is fully studied in [1] at all combustion regimes. The general case is shown in Fig. 7 for RP12. The phase Σ_1 is the burnt gas mixture (shaded in Fig. 7), and Σ_2 is the unburnt one (in white). The velocity of reacting shock wave (RS) is the average interface velocity D_I in Equation (7) of one space dimension. In deflagrations for which the flame visible velocity is calculated by adding the unburnt gas velocity to the imposed fundamental flame speed K_0 , the right genuinely non-linear wave (Rgnl) is the precursor shock wave of the flame (RS), while in detonations (K_0 is not needed), the Rgnl is caught up by the RS, and these two waves overlap in $x-t$ plane. In case of Chapman-Jouguet deflagrations or detonations, a Taylor expansion wave appears behind the reacting shock where the flow is sonic. According to [1] for multi-dimensional case, the velocity of reacting interface is modelled as a function of the fundamental flame speed K_0 and the unburnt gas velocity $\mathbf{v}^{\mathrm{u}}$:

$$\mathbf{D}_I = \mathbf{v}^{\mathrm{u}} + K_0 \mathbf{n} \tag{9}$$

where $\mathbf{n}$ is the normal to the reacting interface going from the burnt gas mixture to the unburnt one. For a multi-dimensional general mesh, as done for the non-reacting case, the average interface velocity in Equation (7) is approximated by the reacting shock velocity normal to each intercell boundary (see [1] for more details).

4 Upwind downwind-controlled splitting

4.1 Considerations for high resolution of interfaces

A predictor-corrector scheme is proposed in [2] in which a second order limited reconstruction is applied to the volume fraction with the aim of improving the interface accuracy. The reconstruction is shown in Fig. 8(a), with the dashed line representing the gradient of the volume fractions. In the DEM approach, it is equivalent to solve the discontinuous representation of the volume fraction inside the computational cell (with full line in Fig. 8(a)). Therefore, a supplementary two-phase Riemann problem is required to be solved inside the cell element as long as its gradient of volume fraction is non-zero. For this reason, when the first order time discretization is concerned, the CFL value should not be larger than $\frac{1}{2}$. However, this time step restriction can be extended up to CFL ≤ 1, if a predictor-corrector type scheme is employed, such as the one proposed in [2, 5]. Thanks to this internal reconstruction of the volume fractions, the interface is numerically less diffused since one part of the generated volume at $x_{i+\frac{1}{2}}$ remains inside the element i, while with a first order method, the entire volume generated at $x_{i+\frac{1}{2}}$ is accumulated inside the element $i+1$, graphically translating the numerical dissipation for the transport equation (7).
A further extension of this MUSCL-type approach has been performed in [5]. An anti-diffusive (downwind-controlled) reconstruction is coupled with the RDEM method with the aim of simulating reacting interface at all combustion regimes. This coupling works well for detonations, however fails for deflagrations. The reconstruction proposed in [5] is illustrated in Fig. 8(b): it also requires the solution of an internal Riemann problem. The difficulty in that case is that the internal discontinuity must be situated "very close" to the intercell boundary, according to the anti-diffusive strategy [4]. In case of deflagrations, the precursor shock wave generated by the internal reactive Riemann problem [1] travels across the intercell boundary, which is not taken into account in [5] . This is the reason why this coupling of an anti-diffusive approach with RDEM is unstable for deflagrations. On the other hand, as far as the detonation is concerned, the reacting interface travels at the same speed as the precursor shock wave, and the stability condition is therefore respected.
To solve this robustness issue when coupling RDEM with an anti-diffusive method, an original upwind downwind-controlled splitting (UDCS) approach is now proposed.

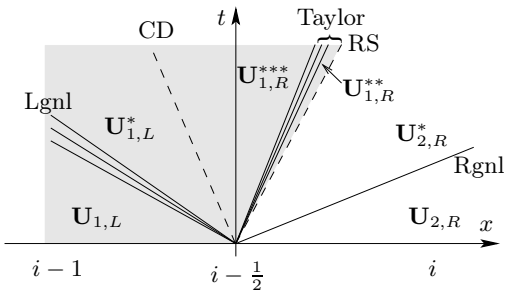

Figure 7: General case of two-phase reactive local Riemann problem RP12($\mathbf{U}^n_{1,i-1}, \mathbf{U}^n_{2,i}; K_0$) at intercell position $x_{i-\frac{1}{2}}$ [1]. The left side is the burnt phase Σ_1, and the right side is the unburnt phase Σ_2. The solution structure contains a left genuinely non-linear wave (Lgnl), a contact discontinuity (CD), a Taylor expansion wave in case of Chapman-Jouguet deflagration or detonation, a reacting shock wave (RS), and a right genuinely non-linear wave (Rgnl). The velocity of reacting shock is the interface velocity D_I in transport equation (7).

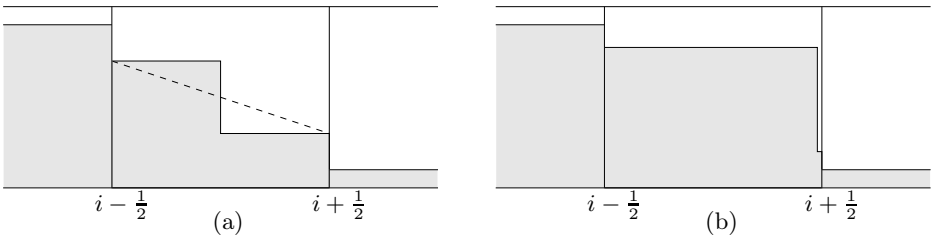

Figure 8: Quasi second order reconstruction (a) for the volume fraction in [2]; anti-diffusive reconstruction (b) in [5].

4.2 Description of the upwind downwind-controlled splitting approach

For the sake of simplicity, the upwind downwind-controlled splitting (UDCS) approach is qualitatively presented in this section for the one dimensional case. The full description for multi-dimensional unstructured problem can be found in Appendix A. The phase index k is omitted in the following.
One of the key underlying idea in devising UDCS is to set robustness as a main priority in the solution procedure. First of all, the first order upwind method is employed in the DEM/RDEM approach for the discretization of the volume fractions (Fig. 9(a)). The separated averaging of conservative variables and volume fraction for both phases is then carried out (Fig. 9(b)). Next, with the aim of improving the volume fraction accuracy, the numerically diffused volumes are displaced back to the upwind cell elements (Fig. 9(c)), preserving the conservative properties of all conservative variables for both phases. Furthermore, this displacement process of the phase volumes should, at the same time, respect the Local Extremum Diminishing (LED) property [24] of the numerical scheme. Additionally, the corresponding conservative variables for these volumes should also be determined.
Let us assume for the sake of demonstration that the interface velocities at location $x_{i-\frac{1}{2}}$ and $x_{i+\frac{1}{2}}$ are both positive (the analysis for other cases is similar). Thus, the intercell boundary $x_{i-\frac{1}{2}}$ is an inlet for both phases in cell i; on its other side, $x_{i+\frac{1}{2}}$ is an outlet. According to the first order upwind method for (7), the inlet

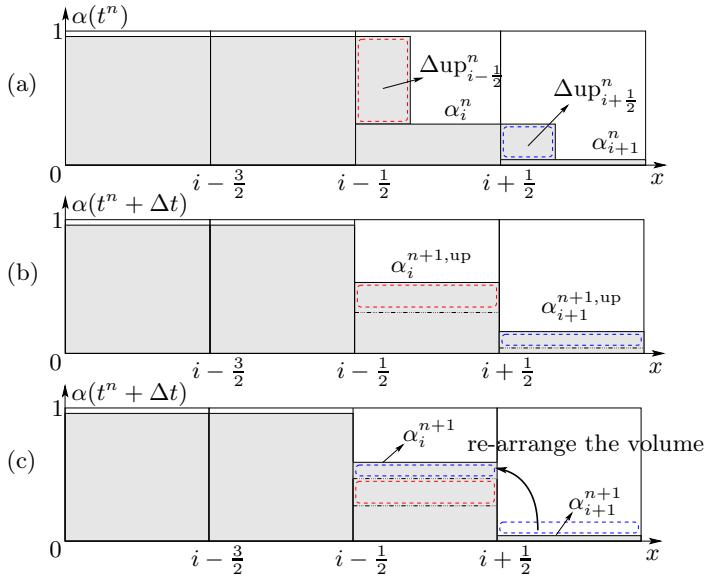

Figure 9: UDCS approach. (a) first order upwind DEM approach involving interface evolution according to the two-phase Riemann problem solution. (b) separated averaging procedures for each phase. (c) phase displacement of UDCS approach determined by the LED property.

and the outlet interfaces at each time step globally "generate" the following volumes (Fig. 9(a)):

$$\begin{aligned}\Delta \mathrm{up}^n_{i-\frac{1}{2}} &= \left(\alpha^n_{i-\frac{1}{2}} - \alpha^n_i\right) D^n_{i-\frac{1}{2}} \Delta t \overset{\text{upwind}}{=} \left(\alpha^n_{i-1} - \alpha^n_i\right) D^n_{i-\frac{1}{2}} \Delta t, \\ \Delta \mathrm{up}^n_{i+\frac{1}{2}} &= \left(\alpha^n_i - \alpha^n_{i+\frac{1}{2}}\right) D^n_{i+\frac{1}{2}} \Delta t \overset{\text{upwind}}{=} \left(\alpha^n_i - \alpha^n_{i+1}\right) D^n_{i+\frac{1}{2}} \Delta t.\end{aligned} \tag{10}$$

where $D^n_{i-\frac{1}{2}}$ and $D^n_{i+\frac{1}{2}}$ are the interface velocity at time t^n given by the local two-phase Riemann problem at $x_{i-\frac{1}{2}}$ and $x_{i+\frac{1}{2}}$, respectively (Section 3.2 and 3.3). $\alpha^n_{i-\frac{1}{2}}$ and $\alpha^n_{i+\frac{1}{2}}$ are interface values for volume fractions at time t^n, and within the framework of upwind method, they are given by values of the upwind cell elements (formulation (10)). As mentioned above for considerations of displacement of phase volumes, in the high order scheme here designed for (7), the quantity of volume kept inside the cell is imposed as follows,

$$\alpha^{n+1}_i = \alpha^n_i + \frac{1-\lambda^n_{i-\frac{1}{2}}}{\Delta x} \underbrace{\left(\alpha^n_{i-1} - \alpha^n_i\right) D^n_{i-\frac{1}{2}} \Delta t}_{\Delta \mathrm{up}^n_{i-\frac{1}{2}}} + \frac{\lambda^n_{i+\frac{1}{2}}}{\Delta x} \underbrace{\left(\alpha^n_i - \alpha^n_{i+1}\right) D^n_{i+\frac{1}{2}} \Delta t}_{\Delta \mathrm{up}^n_{i+\frac{1}{2}}}, \tag{11}$$

with $0 < \lambda^n_{i-\frac{1}{2}},\ \lambda^n_{i+\frac{1}{2}} < 1$. Note that if setting $\lambda^n_{i-\frac{1}{2}} = \lambda^n_{i+\frac{1}{2}} = 0$, formulation (11) degenerates to the upwind scheme for (7), and if setting $\lambda^n_{i-\frac{1}{2}} = \lambda^n_{i+\frac{1}{2}} = 1$ in (11), an unconditionally unstable downwind scheme is recovered for (7). The UDCS for volume fraction transport equation (7) consists now in determining the values of $\lambda^n_{i-\frac{1}{2}},\ \lambda^n_{i+\frac{1}{2}}$ in (11) for a high resolution of the interface.

First of all, a second order reconstruction can be used to calculate λ^n; for instance, at the outlet boundary $x_{i+\frac{1}{2}}$:

$$\lambda^n_{i+\frac{1}{2}} = \frac{\alpha^n_i - \alpha^n_{i+\frac{1}{2}}}{\alpha^n_i - \alpha^n_{i+1}},\ \text{when } \alpha^n_i \neq \alpha^n_{i+1}, \tag{12}$$

with $\alpha^n_{i+\frac{1}{2}}$ the interface reconstructed value at $x_{i+\frac{1}{2}}$ using TVD limiting within element i. It is emphasized that (12) inserted into (11) is equivalent to the conventional second order limiting method for (7) (Fig. 8(a)) if the transport velocity D_I is constant. However, when D_I is obtained by resolving local Riemann problems, these two quasi second order approaches differ from each other.

Alternatively, the downwind-controlled (anti-diffusive) approach [4] can be used to evaluate the values of λ^n in (11) which are in general larger than the ones with TVD limiters. Using the inlet interfaces, one needs to compute the minimum and maximum values of m^n and M^n for each cell element, such that

$$\begin{aligned} m^n_i &= \min\left\{\alpha^n_i, \alpha^n_{i-1}\right\}, \\ M^n_i &= \max\left\{\alpha^n_i, \alpha^n_{i-1}\right\}. \end{aligned}$$

The LED property requires to ensure $m^n_i \leq \alpha^{n+1}_i \leq M^n_i$, that is:

$$m^n_i \leq \alpha^n_i + \frac{1-\lambda^n_{i-\frac{1}{2}}}{\Delta x} \Delta \mathrm{up}^n_{i-\frac{1}{2}} + \frac{\lambda^n_{i+\frac{1}{2}}}{\Delta x} \Delta \mathrm{up}^n_{i+\frac{1}{2}} \leq M^n_i. \tag{13}$$

Formula (13) represents a difficult linear system of inequalities to solve since it globally involves all λ^n in the computational domain. According to [4], tolerated values can be used as a sufficient condition to satisfy these linear inequalities. A similar strategy is used in the present work to eliminate this difficulty. Details about the tolerated values of λ^n used in this work can be found in Appendix A . In brief, one of the two λ^n in (13) is replaced by a fixed value still guaranteeing these inequalities, which allows to simply determine the largest value of λ^n. The values of λ^n thus obtained are certainly not the largest ones in the algebraic sense, but this approach gives the practical possibility of determining the required values of λ^n locally. Furthermore, its simplicity makes the UDCS method very easy to implement.

4.3 Implementation into the DEM/RDEM

The numerical scheme developed in Section 4.2 for the volume fraction transport equation (7) in the two-phase flow model can be easily implemented into the (Reactive) Discrete Equations Method. As already mentioned in Section 4.1, in order to guarantee the method robustness, the first order upwind method for the volume fraction is, first of all, processed in the DEM/RDEM approach (Fig. 9(a)). The conservative variables of each phase are consequently updated after upwinding (state denoted $\mathbf{U}_k^{n+1,\mathrm{up}}$) using separated averaging procedure described in Section 3 (Fig. 9(b)). Then, following the strategy described in Section 4.2, the corresponding volumes of each phase are globally rearranged in the computational domain using the formulae (11) and the appropriate values of λ^n (second order or downwind-controlled) at each intercell boundary (Fig. 9(c)).
The only remaining issue in the upwind downwind-controlled splitting approach is to determine how assigning the conservative variables to the corresponding moving volumes of each phase. A possible approach is to associate the phase volumes being displaced and rearranged with the conservative variables $\mathbf{U}_k^{n+1,\mathrm{up}}$ after the upwind approach of DEM/RDEM. This numerical technique takes advantage of stability property of the upwind scheme, and a wide range of numerical experiments involving both reacting and non-reacting flows show that this simple association is numerically sufficient. Indeed, the corresponding results are oscillation free and very accurate near the interface. The simplicity of this technique makes UDCS very convenient for implementation in existing CFD codes.
A distinct difference between UDCS and a standard high resolution method is that UDCS works on the system variables to achieve high accuracy instead of working on the numerical flux; this feature plays a key role in preventing the occurrence of robustness issues for UDCS.

5 Numerical results

5.1 One dimensional non-reacting water gas shock tube problem

Let us consider the water-gas shock tube previously proposed in [25], with stiffened gases thermodynamic closures. The main challenge of this test-case is to overcome the numerical robustness issue which usually appear when computing the strong rarefaction wave created when the high pressurized water on the left is put in contact with the gas at atmospheric pressure on the right.
At initial state, the high pressure (10^9 Pa) left chamber ($0 \leq x \leq 0.7$ m) contains nearly pure water and a small volume of gas (volume fraction $\varepsilon = 10^{-8}$) while the low pressure (10^5 Pa) right chamber contains nearly pure gas with a small amount of water (volume fraction $\varepsilon = 10^{-8}$). The gas density is 10 kg/m^3 in the whole domain, while the water density is 1000 kg/m^3. Both fluids are initially at rest. The EOS parameters are set equal to $\gamma = 1.4$, $p_\infty = 0$ for the gas and $\gamma = 4.4$, $p_\infty = 6.0 \times 10^8$ Pa for water.
A 2-step Runge-Kutta method is used for the time discretization; density, velocity and pressure are reconstructed using the minmod limiter in order to achieve (quasi) second order accuracy in space. As far as the the phase volume fraction is concerned, "UDCS anti" combines DEM (usual formulation), UDCS and the anti-diffusive approach; "2-nd minmod" makes use of the (quasi) second order DEM proposed in [2], with minmod reconstruction. Numerical results obtained by combining DEM, UDCS and the minmod reconstruction for the phase volume fraction are not shown since they almost coincide with the ones obtained using the second order DEM proposed in [2]. The computed results are compared to the available exact solution of the problem.
The results displayed in Fig. 10 are obtained on a uniform mesh of 100 cells. With only one point in the material interface zone, the anti-diffusive UDCS demonstrates its capacity to "exactly" capture the interface, which makes it more accurate than the second order DEM scheme. Examining the Mach number results, it is observed the supersonic part of flow is well resolved by the UDCS method while spurious subsonic results are obtained using the second order DEM scheme. If using a uniform mesh with 1000 cells (Fig. 11) perfect agreement is obtained between the numerical and exact solutions. The numerical results obtained using the anti-diffusive UDCS method are more accurate at the interface than the ones in [25]. All the computed variables are oscillation free, including the Mach number. The under-shoot in the pressure profile at the end of the rarefaction wave is linked to the high pressure ratio in the rarefaction wave, which cause some numerical approaches (but not the one proposed here) to fail in computing this test case.

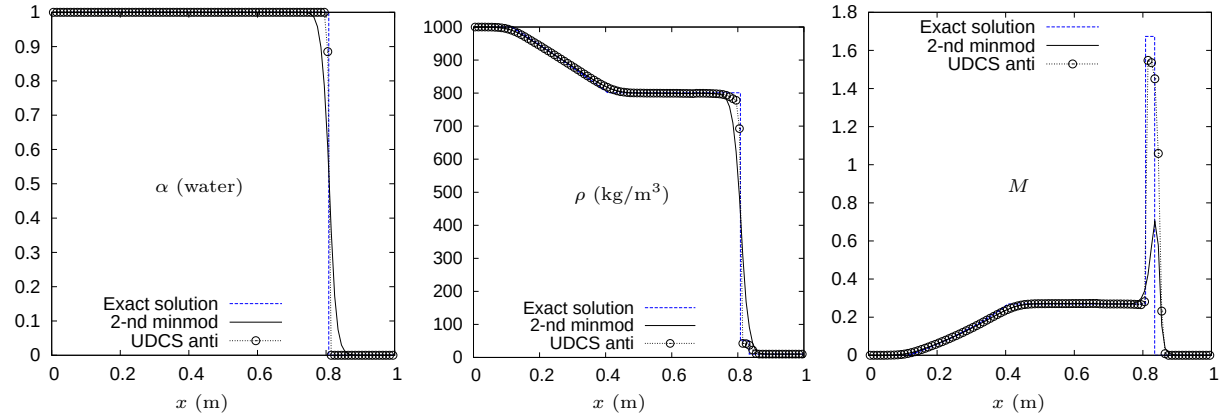

Figure 10: Water gas shock tube problem with interface separating two phases. DEM method is used. UDCS anti-diffusive solutions compared with second order scheme in [2] with minmod limiter. A 100 cells mesh is used. CFL = 0.9. Time $t = 220$ μs. The exact solutions are shown in dashed blue lines.

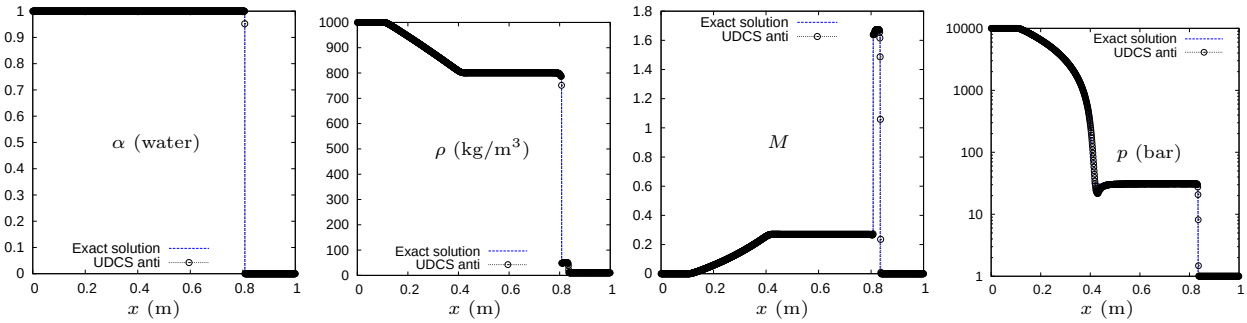

Figure 11: Water gas shock tube problem with interface separating two phases. DEM method is used. UDCS anti-diffusive solutions compared with exact solutions. A 1000 cells mesh is used. CFL = 0.9. Time $t = 220$ μs. The exact solutions are shown in dashed blue lines.

5.2 One dimensional Chapman-Jouguet deflagration

Let us consider the Chapman-Jouguet deflagration shock tube already proposed in [1]. This test case is interesting because it allows observing how the poor accuracy on the flame region can affect the accuracy on the flame-generated shock wave. The 20 meter long shock tube involves on the right (10 m $\leq x \leq$ 20 m) a stoichiometric mixture of hydrogen-air, with pressure and temperature equal to 1.013 bar and 290 K respectively. On the left, the burnt gas (due to the complete combustion of the stoichiometric mixture of hydrogen-air) is found with pressure and temperature equal to 2.013 bar and 2800 K. The specific heats are computed as fourth-degree polynomials of the temperature, obtained by interpolating data in JANAF tables [26]. For the numerical reasons already explained in [2], the right part contains a very small volume of burnt gas (volume fraction is $\varepsilon = 10^{-8}$) and the left part contains a very small volume of unburnt gas (volume fraction is $\varepsilon = 10^{-8}$). The gases are initially at rest.
The exact solution of the reactive Euler equations and the numerical solutions obtained with the RDEM are compared in Fig. 12. As in the non-reacting water gas shock tube problem case, the 2-step Runge-Kutta method is used for the time discretization; density, velocity and pressure are reconstructed using the minmod limiter. As far as the the phase volume fraction is concerned, the denominations "UDCS anti" and "2-nd minmod" have the same meaning as in the previous test case. A uniform mesh of 100 cells is used and the CFL is set equal to 0.75. As illustrated in Fig. 12, "2-no minmod" calculations yield a very diffused interface which in turn exceedingly moderates the maximum over-pressure behind the non-reacting right-travelling shock wave. On the other hand, as for the non-reacting case, the "UDCS anti" approach can "exactly" capture the flame interface, which substantially improves the results on the maximum over-pressure following the

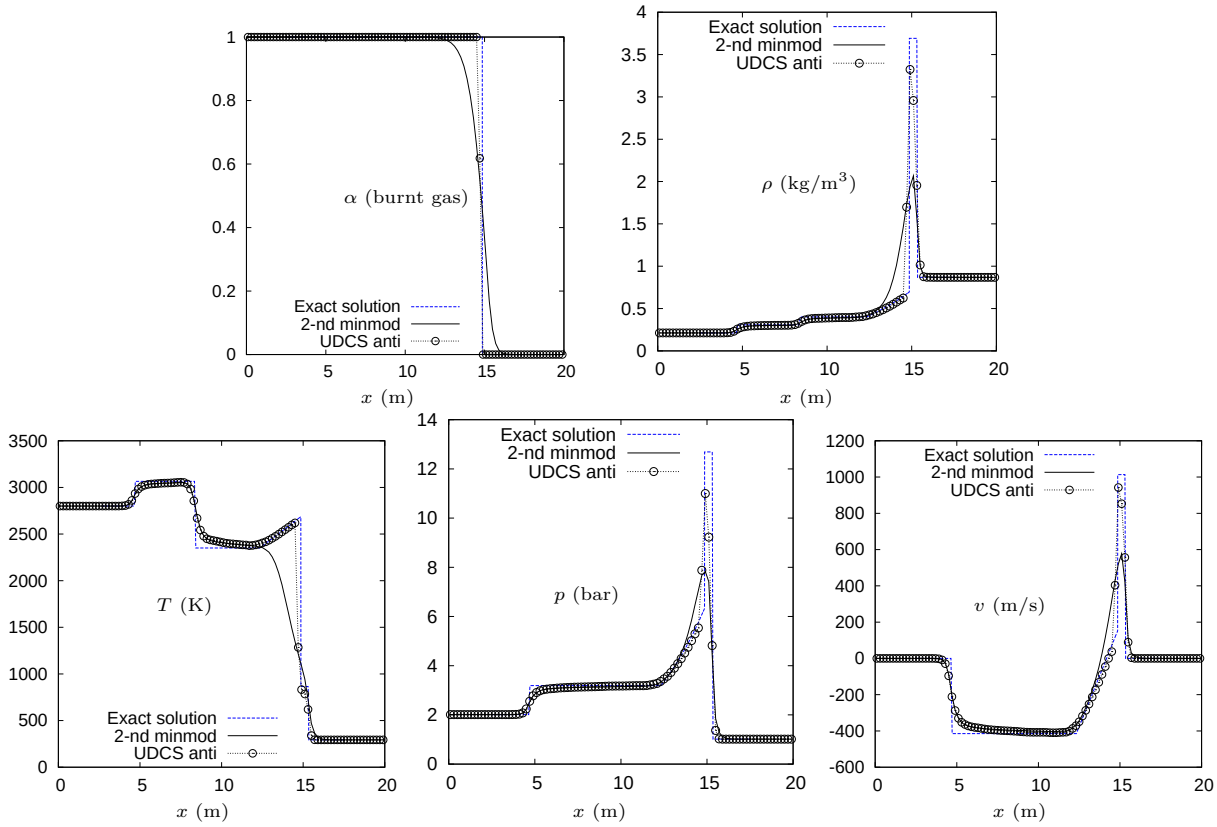

Figure 12: Shock tube of Chapman-Jouguet deflagration. RDEM method is used. UDCS anti-diffusive solutions compared with second order scheme with minmod limiter. A 100 cells mesh is used. CFL = 0.75. Time $t = 4.0$ ms. The exact solutions [1] are shown in dashed blue lines.

non-reacting shock wave. This makes the "UDCS anti" approach a good candidate to perform investigations of fluid-structure interaction problems involving combustion-generated pressure waves.
As in the non-reacting water gas shock tube problem, numerical results obtained by combining UDCS and the minmod reconstruction for the phase volume fraction are not shown since they almost coincide with the ones obtained using the second order DEM proposed in [2] ("2-nd minmod" in the figure). Nevertheless, it should be emphasized that, for this test case, the former approach is more robust than the latter: indeed the second order scheme proposed in [2] does not work for CFL close to unity, while the numerical approaches involving UDCS does.

5.3 Two-dimensional gaseous non-reacting shock bubble interaction

This shock bubble test case is particularly interesting since it has been numerically investigated in several previous works (see for instance [27, 28, 9]). Moreover, experimental results are also available [29].
The flow problem consists in simulating the impact of a Mach 1.22 shock travelling through air (light gas) onto a cylinder of R22 gas (heavy gas). The configuration is shown in Fig. 13. A cylinder of R22 is surrounded by air within a 445×89 mm^2 rectangular domain. At $t = 0$, the cylinder is at rest and its center is located at $(x, y) = (225\text{ mm}, 44.5\text{ mm})$. The initial radius of the cylinder is $r = 25$ mm. The planar shock is initially located at $x = 275$ mm and moves from right to left towards the cylinder. The generated flow illustrates the interaction of a material interface with a shock wave, coming from the light gas region into the heavy gas region. The resulting waves, at the early stage of fluid interaction, include a transmitted shock wave in air, a refracted shock wave in the R22 bubble, a material interface and a reflected shock wave in air. Due to the smaller speed of sound in R22 gas, the refracted shock wave in R22 propagates more slowly than the transmitted shock wave in air.

Both fluids are described by polytropic EOS. Initial conditions and fluid properties are summarized in Table 1. The top and bottom boundary conditions are set as solid walls while constant state boundary conditions are imposed on the left and right boundaries.

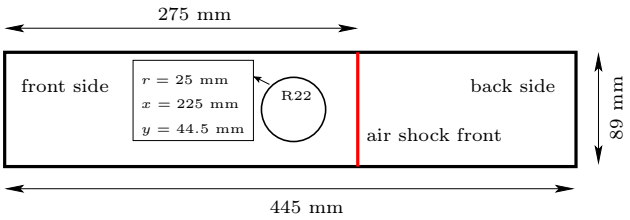

Figure 13: Initial configuration of air-R22 shock problem.

Location	Density (kg m^{-3})	Pressure (Pa)	u_x (m s^{-1})	u_y (m s^{-1})	γ
Air (back side)	1.686	1.59×10^5	-113.5	0	1.4
Air (front side)	1.225	1.01325×10^5	0	0	1.4
R22	3.863	1.01325×10^5	0	0	1.249

Table 1: Air-R22 shock/cylinder interaction test. EOS coefficients and initial data.

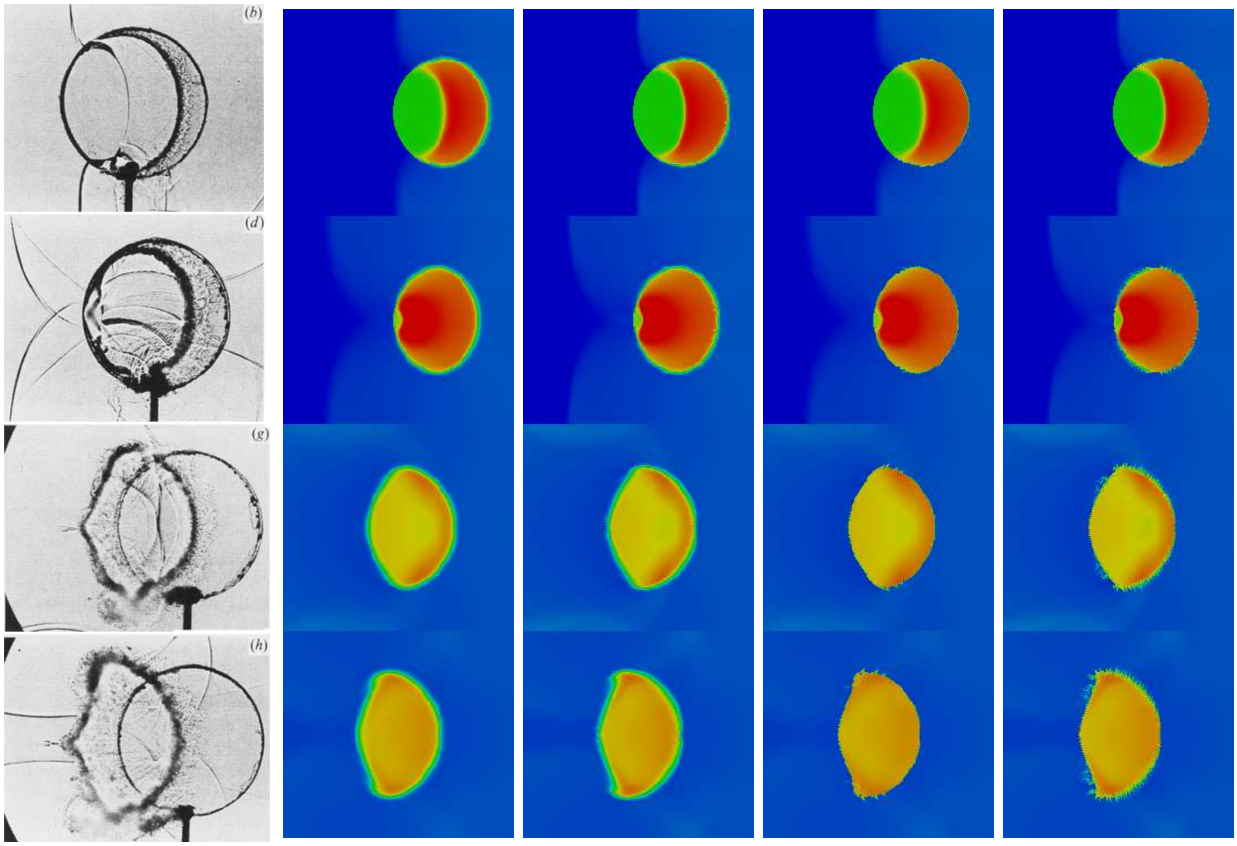

Figure 14: Air-R22 shock/cylinder interaction test. Numerical results of density profile. From left to right: experimental results in [29], UDCS minmod method with 1000×200 Cartesian mesh, UDCS minmod method with triangular mesh of $1000 \times 200 \times 2$ cells, UDCS anti-diffusive method with 1000×200 Cartesian mesh, and UDCS anti-diffusive method with triangular mesh of $1000 \times 200 \times 2$ cells. Five instants are selected from [29]: (b) $t = 115$ μs, (d) $t = 187$ μs, (g) $t = 342$ μs, (h) $t = 417$ μs, (i) $t = 1020$ μs.

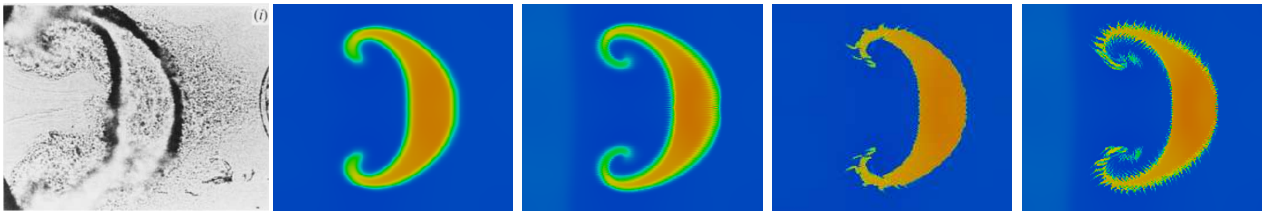

Figure 14: (*continued*)

In Fig. 14, experimental Schlieren images (column 1) taken from [29] are compared with the numerical solutions provided by four different strategies, all relying on DEM but with distinct treatments for the volume fraction equation:

1. UDCS with minmod reconstruction (quasi second order), on a 1000×200 Cartesian mesh (column 2).
2. UDCS with minmod reconstruction, on a $1000 \times 200 \times 2$ triangular mesh (column 3).
3. UDCS and anti-diffusive approach, on a 1000×200 Cartesian mesh (column 4).
4. UDCS and anti-diffusive approach, on a $1000 \times 200 \times 2$ triangular mesh (column 5).

In all cases, the Euler explicit scheme is used for time discretization, with a CFL value set to 0.4. No reconstruction on the primitive variables is performed. As done in [29], the results are shown around the R22 gas bubble at several different times (measured relative to the moment when the shock wave first interacts with the bubble boundary at time $t = 60\ \mu s$): $(b)\ t = 115\ \mu s$, $(d)\ t = 187\ \mu s$, $(g)\ t = 342\ \mu s$, $(h)\ t = 417\ \mu s$, $(i)\ t = 1020\ \mu s$. Qualitatively our numerical results, on both triangular and quadrangular meshes, are in good agreement with the experimental data in [29], and also with previous numerical results in [27, 28, 9]. Moreover the interface resolution is significantly improved when the UDCS anti-diffusive method is employed. It is interesting to notice that the UDCS anti-diffusive method works with unstructured triangular mesh. However, a kind of "capillary" numerical phenomenon is observed in the vicinity of the fluid interface (the dimension of which reduces with the mesh resolution).
The different numerical approaches are also compared by analyzing the volume fraction and the mixture density at the final computational time. The results in Fig. 15 are plotted along the axis of symmetry ($+x$ direction), in the region occupied by the bubble. Three differently refined Cartesian meshes and three differently refined triangular meshes are used for comparison. From a qualitative viewpoint, it can be said that all approaches converge to the same result. More precisely now, one can notice that, on quadrangular meshes, UDCS anti-diffusive approach with 500×100 Cartesian mesh produces more accurate results than UDCS minmod approach with 1000×200 cells. The triangular mesh used in this test is twice finer than the corresponding Cartesian mesh. Results obtained with the triangular mesh are displayed in the third column. The UDCS anti-diffusive approach yields again more accurate results than the UDCS minmod approach.
Further plots (Fig. 17 and Fig. 18) are drawn along the two lines perpendicular to the axis of symmetry (y direction) whose location over the final time bubble shape is indicated in Fig. 16. The grid-convergence of the results can be qualitatively observed and the UDCS anti-diffusive approach still proves to be more accurate than the UDCS minmod approach. In line with the triangular mesh results shown in Fig. 14 for the UDCS anti-diffusive approach, the "capillary" interface profile is visible in the third column of Fig. 17 and Fig. 18.
Finally, the pressure time-history is shown in Fig. 19 for the sake of comparison with [27, 28, 9, 29]. Three locations are retained: $x_p = 3,\ 27,\ 67$ mm, downstream of the R22 gas bubble along the axis of symmetry. Time is measured from the first communication of the shock wave with the bubble at time $t = 60\ \mu s$. UDCS anti-diffusive results on triangular mesh of $250 \times 50 \times 2$, $500 \times 100 \times 2$, and $1000 \times 200 \times 2$ elements are presented so that grid convergence can be qualitatively checked. No noticeable difference is observed when comparing the results obtained with the UDCS minmod method and the UDCS anti-diffusive method on the same mesh. Note that pressure peaks are not resolved as accurately as in [9], where a more refined mesh was used. Moreover, it is worthwhile to mention that, with a fixed CFL value, considerably more time steps are required for computations with fully non-equilibrium model of two-fluid flow than with a sub-model, such

as the one used in [9] (more information can be found in [18]). This can generally make results of two-fluid model more diffused than the ones of a sub-model.

5.4 2D computation of 1D line-symmetric steady combustion

This test case has been previously considered in [1], Section 6.3, page 300. It consists in propagating a 1D line-symmetric deflagration wave in a 2D domain, initially filled with a stoichiometric mixture of (thermally perfect) hydrogen-air at rest. Its interest is linked to the fact that the analytical solution (see for instance [30]) can be evaluated; alternatively, a reference solution can be obtained by performing a 1D line-symmetric computation (as done here). It is emphasized that this solution for the multi-dimensional Euler equations is, in reality, unstable (the stability of a cylindrical/spherical flame is guaranteed by the competition between thermal and species diffusion, which is neglected in the Euler equations). Nonetheless, this solution can be used as a comparison from a qualitative viewpoint. From now on, the 1D line-symmetric solution will be referred to as the "reference solution".
As far as initial conditions are concerned, initial pressure and temperature are assumed respectively equal to 1.013 bar and 290 K. The fundamental speed is $K_0 = 45.2$ m/s.
As shown in [1], when observing the solution obtained using the original RDEM on a quadrangular regular mesh, it can be noticed that the flame propagates at different speeds on the diagonal and on the axis. In our opinion, this is due to the fact that, when studying 1D reactive Riemann problems at the cell interfaces, the cell interface normal ($\mathbf{n}_f$) can be different from the flame surface normal ($\mathbf{n}$)[1]. As shown in [1], if in evaluating the solution of the 1D reactive Riemann problem, the fundamental flame speed is supposed to be

[1]Let us recall that the total flame velocity is $\mathbf{D}_I = \mathbf{v}^{\mathrm{u}} + K_0\mathbf{n}$, (see equation (9))

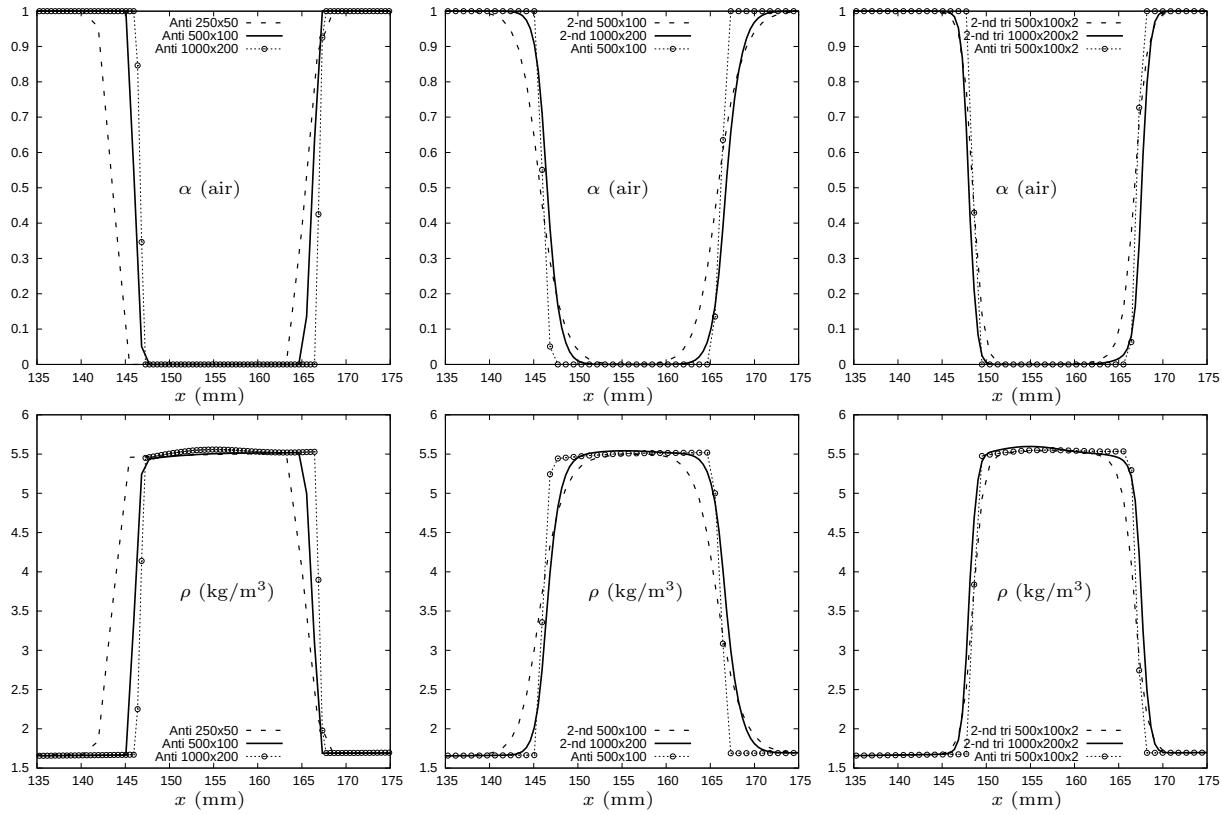

Figure 15: Plottings of volume fraction and mixture density over the axis of symmetry (x direction) around the R22 bubble. Anti stands for UDCS anti-diffusive approach. 2-nd stands for UDCS minmod approach (which is quasi second order). tri stands for triangular mesh.

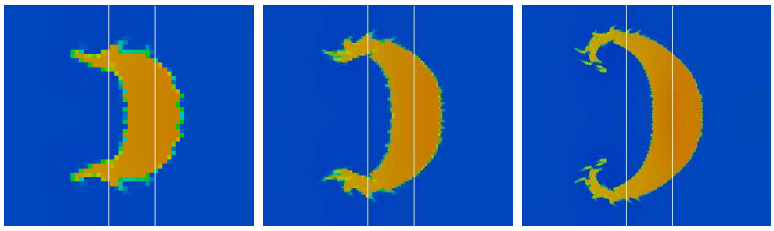

Figure 16: Positions of y direction lines for plottings of volume fraction and mixture density in Fig. 17 and Fig. 18. From left to right: UDCS anti-diffusive approach with Cartesian mesh of 250×50, 500×100, and 1000×200 cells. Left line is located at $x = 136$ mm, and right line at $x = 155$ mm (measured from the left boundary of the whole domain).

given by $K_0|\mathbf{n} \cdot \mathbf{n}_f|$ (instead of K_0), directional effects drastically reduce. This strategy will be adopted in the following.

Let us now compute the solution on a regular grid of 400×400 elements and a CFL equal to 0.4. The combustion is "numerically initiated" by supposing that in the closest element to the center of symmetry (the left bottom corner in Fig. 20), the mixture is burnt (here initial pressure and temperature are equal to 2.013 bar and 2800 K but it must be emphasized that these values do not significantly affect the solution). In Fig. 20 (first three lines) we represent the solution at 1.2 ms, obtained with different approaches: the RDEM approach (explicit Euler scheme for time discretization), the RDEM approach with minmod reconstruction

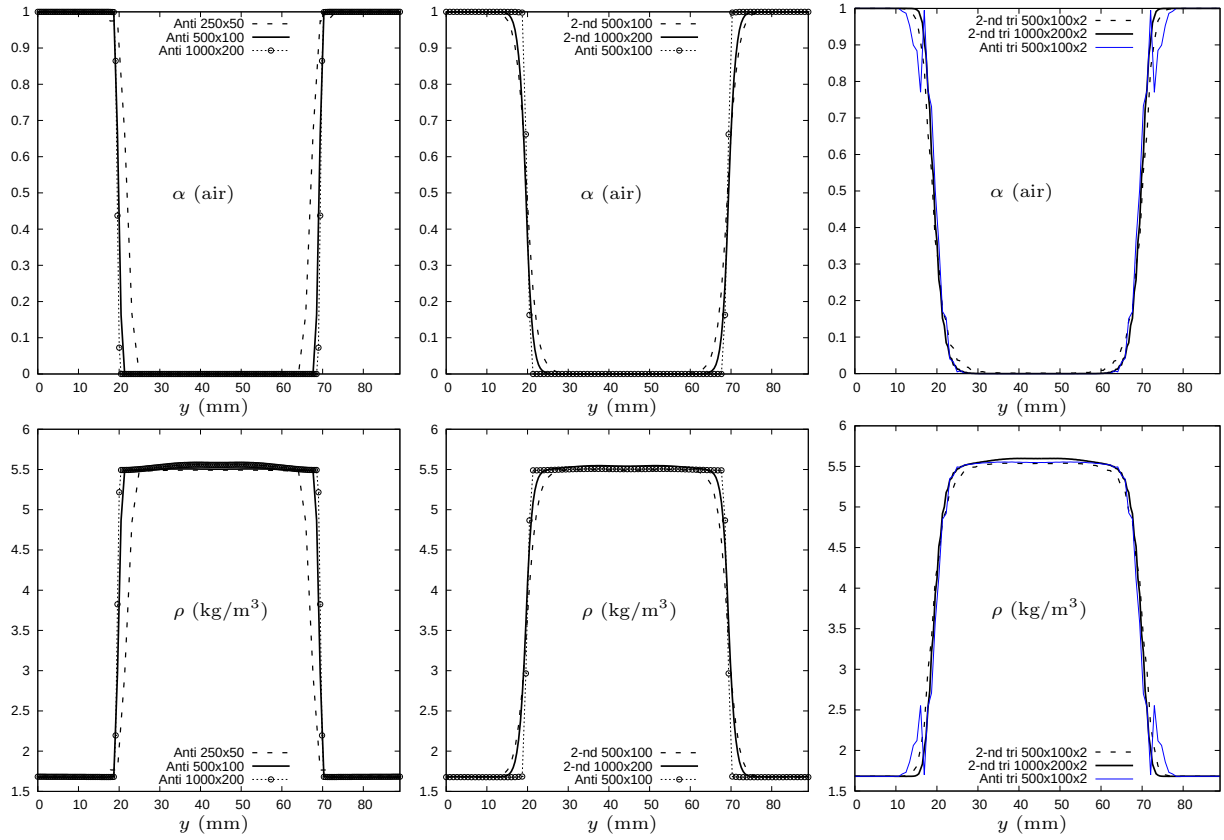

Figure 17: Plottings of volume fraction and mixture density over the line situated at $x = 155$ mm (Fig. 16). Anti stands for UDCS anti-diffusive approach. 2-nd stands for UDCS minmod approach (which is quasi second order). tri stands for triangular mesh.

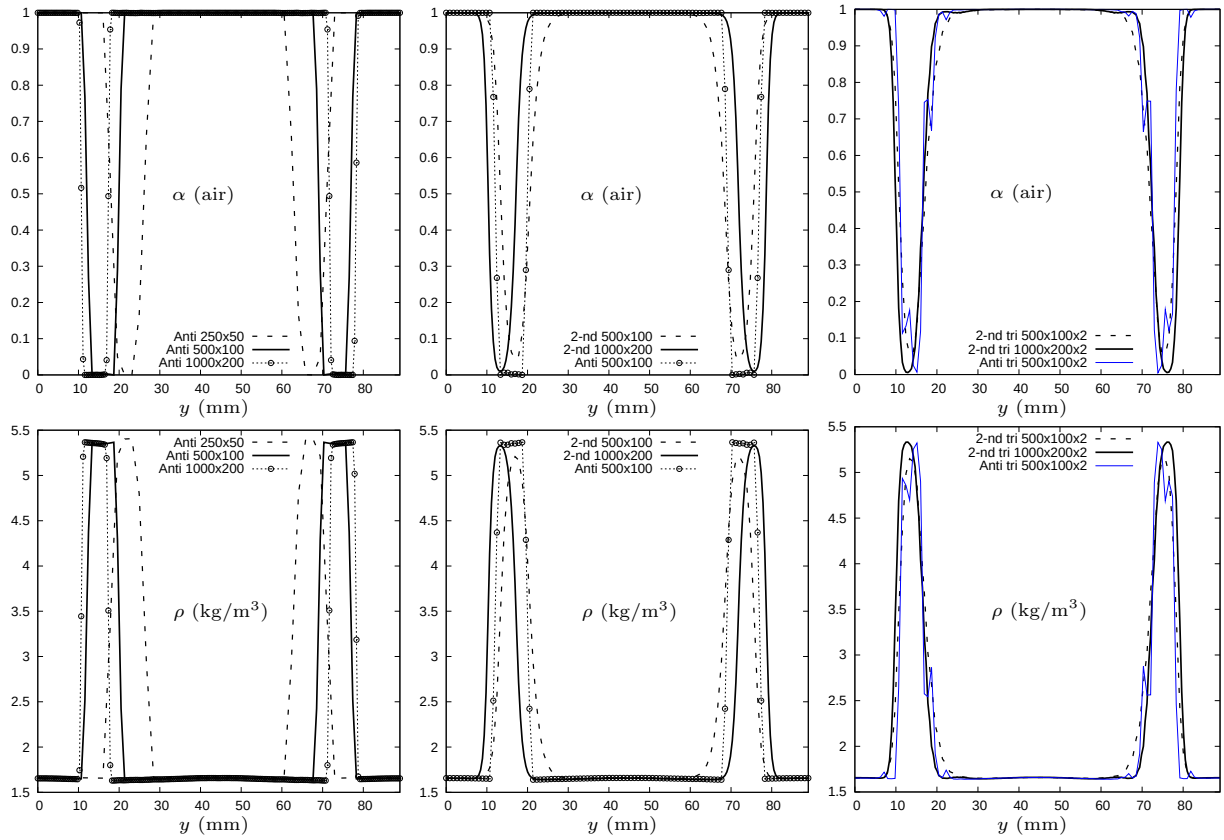

Figure 18: Plottings of volume fraction and mixture density over the line situated at $x = 136$ mm (Fig. 16). Anti stands for UDCS anti-diffusive approach. 2-nd stands for UDCS minmod approach (which is quasi second order). tri stands for triangular mesh.

on pressure, density, velocity and volume fraction (second order explicit Runge-Kutta scheme for time discretization), and the (RDEM) UDCS anti-diffusive approach (explicit Euler scheme for time discretization). On the left we represent the volume fraction of the burnt gas and the pressure. On the right we plot the results thus obtained on the axis and on the diagonal. As one can see, the results closest to the reference

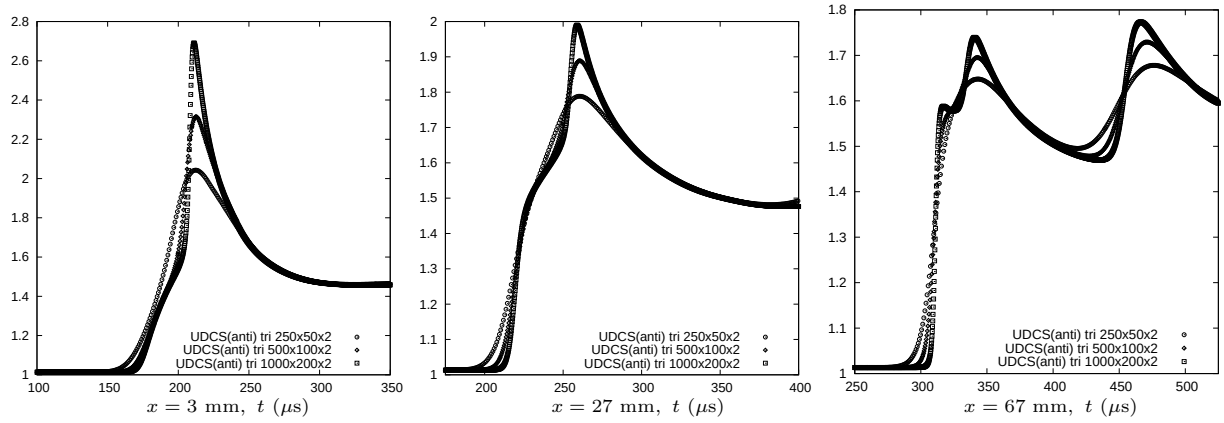

Figure 19: Time history of pressure in three locations: $x = 3$ mm, $x = 27$ mm, and $x = 67$ mm downstream of the R22 gas bubble along the axis of symmetry. Anti stands for UDCS anti-diffusive approach. tri stands for triangular mesh.

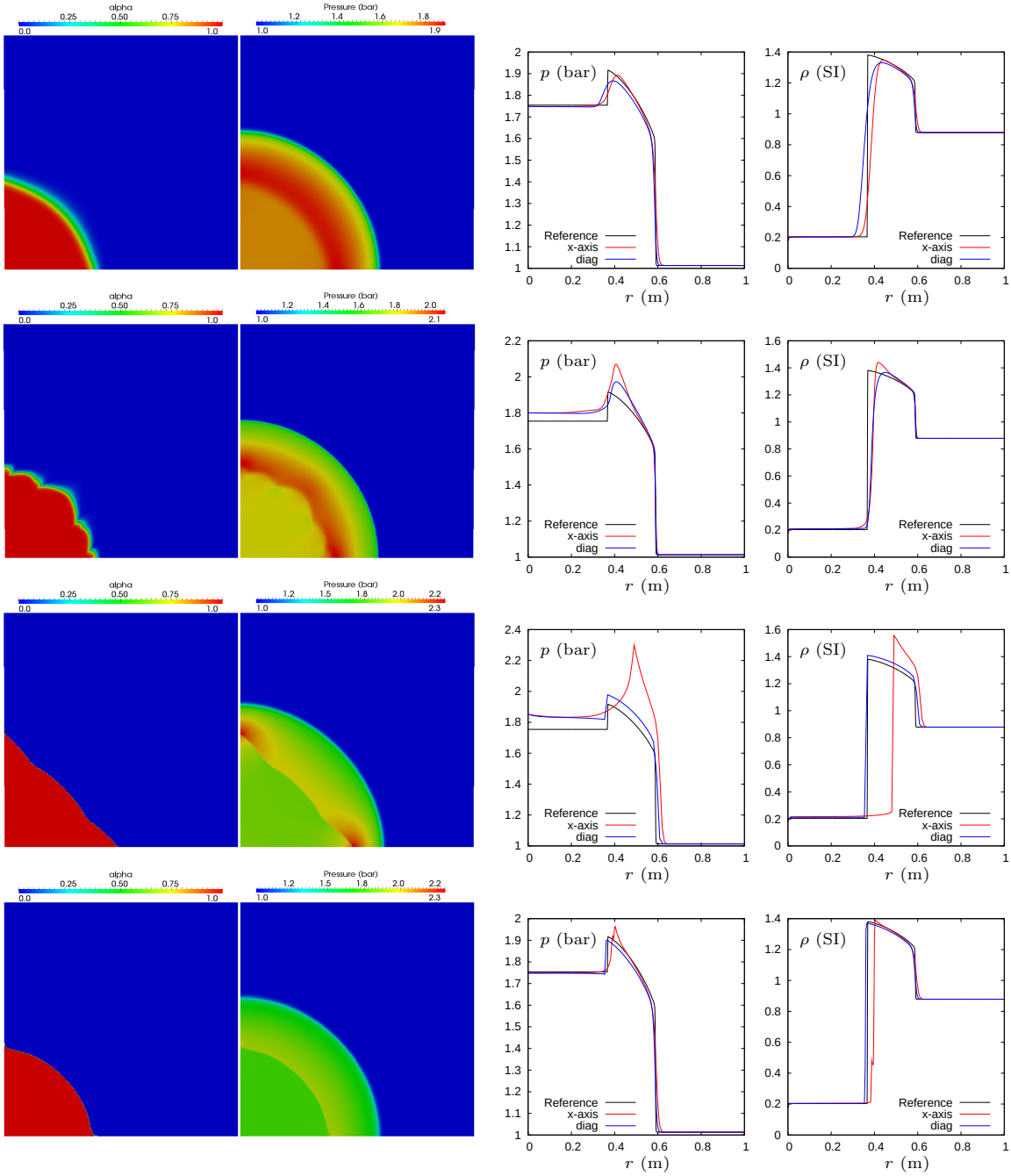

Figure 20: Propagation of a 1D line-symmetric steady flame. On the top (first line), first order RDEM (explicit Euler scheme for time discretization). On the second line quasi-second order UDCS, with minmod reconstruction for all primitive variables (second order explicit Runge-Kutta scheme for time discretization). On the third line, the UDCS anti-diffusive approach (explicit Euler scheme for time discretization). On the fourth line, the UDCS anti-diffusive approach (explicit Euler scheme for time discretization), in which normals at the flame interface are forced to be equal to the ones at the reference solution (namely $\mathbf{n} = (x/r, y/r)$). From left to right: the volume fraction of the burnt gas, the pressure, the plottings of pressure over axis and diagonal, and that of density. The reference solution is obtained using a 1D line-symmetric solver and the UDCS anti-diffusive approach.

solution are the ones given by the first order RDEM (which present the highest numerical diffusion). The results obtained using the minmod reconstruction are less diffused than the ones given by the first order reconstruction. As observed, the propagation speed of the flame on the axis and on the diagonal is almost the same. The flame interface shape is not circular; this is expected, since the reference solution is unstable. Pressure and density are higher than the ones given by the first order approach. This is due to the fact that as the flame surface wrinkles, the quantity of unburnt gas which burns per time unit increases. This increases in turn the release of chemical energy per time unit and thus the pressure (as can be checked in Fig. 20, pressure is slightly higher than the reference one). Finally, in the UDCS anti-diffusive solution it is noticed that the volume fraction is less diffused than the other solutions but the flame is much faster on the axis than on the diagonal. This point will be investigated in the future and it is maybe due to that the flame interface normal evaluation with the formula $\nabla(\alpha)/|\nabla(\alpha)|$ creates problems when α is not smooth. This assertion is confirmed by the results shown in the fourth line of Fig. 20, in which we have forced the flame interface normal to be equal to the one of the 1D line-symmetric solution (namely $\mathbf{n} = (x/r, y/r)$). In this case, the propagation velocities are almost the same on all directions (and the solution is less diffused than in the other approaches, as expected).

6 Conclusions & perspectives

This paper has described a new computational strategy with the aim of treating the interface problems, based on the (Reactive) Discrete Equations Method (DEM/RDEM). When compared to the literature for anti-diffusive type method [9], the proposed upwind downwind-controlled splitting (UDCS) strategy coupled with DEM/RDEM is capable of dealing with permeable fronts, particularly all speed reacting fronts in our applications. Both accuracy and robustness have been successfully ensured. Indeed, the UDCS approach (either second order limited or anti-diffusive) is proved as stable as first order upwind method. Moreover, higher computational efficiency is also achieved. Indeed, the internal Riemann problem calculated within the classical second order limiting approach [2] is no longer needed when using UDCS method. The steeper representation of the interface also reduces the zone where expensive two-phase Riemann problems have to be computed with DEM/RDEM. This second point can lead to computations that become more efficient than first order simulations.
It is emphasized that the limiting second order UDCS has already been combined with a second order explicit Runge-Kutta approach for time discretization. This allows to work with acceptable CFL using a limiting second order reconstruction on primitive variables (to be quasi-second order in space and time on the whole variables). Unfortunately, it is not so easy to couple the anti-diffusive UDCS with the explicit second order Runge-Kutta scheme; this point should be investigated in the future. Moreover, as already mentioned, it should also be necessary, in the future, to change our approach to compute the normal at the flame interface. Finally, although our approach of UDCS is proposed for the full non-equilibrium two-fluid model, we believe that it is worthwhile to extend this concept to sub-models of two-phase flow for interface computations.

Acknowledgements

This work is supported by the French Atomic Energy and Alternative Energies Commission (CEA).

Appendix A Multi-dimensional UDCS

For simplicity, two-dimensional case is presented here. the phase index k is omitted in this section. Indeed, the scheme of UDCS is the same for both phases. It is emphasized here that only considerations for the volume fraction α is shown below. The implementation into the DEM/RDEM approach is already explained in Section 4.
An unstructured two-dimensional element $\mathcal{C}_i$ is shown in Fig. 21. Its boundaries $\{\partial\mathcal{C}_{i,j}\}$ are divided into two categories: *inlet* (noted as $\{\partial\mathcal{C}_{i,\text{in},j}\}$) and *outlet* (noted as $\{\partial\mathcal{C}_{i,\text{out},j}\}$) ones. An inlet boundary $\partial\mathcal{C}_{i,\text{in},j}$ for phase Σ_k is characterized by $\mathbf{D}^n_{i,\text{in},j} \cdot \mathbf{n}_{i,\text{in},j} < 0$, with $\mathbf{n}_{i,\text{in},j}$ the normal vector pointing toward the outside

of $\mathcal{C}_i$. That is, the interface enters inside $\mathcal{C}_i$, which generates a (positive or negative) volume of Σ_k. On the other hand, it is an outlet boundary $\partial\mathcal{C}_{i,\text{out},j}$, when $\mathbf{D}^n_{i,\text{out},j} \cdot \mathbf{n}_{i,\text{out},j} > 0$.
A classical upwind type scheme for the transport equation (7) can be written as

$$\alpha_i^{n+1} = \alpha_i^n + \sum_j \frac{\Delta \text{up}^n_{i,\text{in},j}}{|\mathcal{C}_i|}, \tag{14}$$

with $|\mathcal{C}_i|$ the volume of $\mathcal{C}_i$ and $\Delta \text{up}^n_{i,\text{in},j}$ the volume of Σ_k entering into $\mathcal{C}_i$ through the inlet boundary $\partial\mathcal{C}_{i,\text{in},j}$ and defined by

$$\Delta \text{up}^n_{i,\text{in},j} = \left(\alpha^n_{i,\text{in},j} - \alpha^n_i\right) |\partial\mathcal{C}_{i,\text{in},j}| \left|\mathbf{D}^n_{i,\text{in},j} \cdot \mathbf{n}_{i,\text{in},j}\right| \Delta t, \tag{15}$$

with $|\partial\mathcal{C}_{i,\text{in},j}|$ the interfacial surface area of $\partial\mathcal{C}_{i,\text{in},j}$. The upwind formulation (14) can be rearranged as follows:

$$\alpha_i^{n+1} = \alpha_i^n \Big(1 - \frac{\Delta t}{|\mathcal{C}_i|} \sum_j |\partial\mathcal{C}_{i,\text{in},j}| \left|\mathbf{D}^n_{i,\text{in},j} \cdot \mathbf{n}_{i,\text{in},j}\right|\Big) + \sum_j \alpha^n_{i,\text{in},j} \Big(\frac{\Delta t}{|\mathcal{C}_i|} |\partial\mathcal{C}_{i,\text{in},j}| \left|\mathbf{D}^n_{i,\text{in},j} \cdot \mathbf{n}_{i,\text{in},j}\right|\Big). \tag{16}$$

When imposing, in practical computations, the time step Δt like,

$$\Delta t \leq \min_i \frac{|\mathcal{C}_i|}{\sum_j |\partial\mathcal{C}_{i,\text{in},j}| \left|\mathbf{D}^n_{i,\text{in},j} \cdot \mathbf{n}_{i,\text{in},j}\right|}, \tag{17}$$

α_i^{n+1} in (16) can thus be viewed as an average value among α_i^n and $\{\alpha^n_{i,\text{in},j}\}$ of its inlet neighbors $\{\mathcal{C}_{i,\text{in},j}\}$, which obviously respect the local Extremum Diminishing (LED) property [24]:

$$\alpha_i^{n+1} \in [m_i^n, M_i^n]. \tag{18}$$

The local maximum and minimum values for $\mathcal{C}_i$ in (18) are computed as follows:

$$m^n_{i,\text{in},j} = \min\{\alpha_i^n, \alpha^n_{i,\text{in},j}\},\ M^n_{i,\text{in},j} = \max\{\alpha_i^n, \alpha^n_{i,\text{in},j}\},$$

$$m_i^n = \min_j\{m^n_{i,\text{in},j}\},\ M_i^n = \max_j\{M^n_{i,\text{in},j}\}.$$

It is worthwhile to notice that, if only viewing the scalar equation (7), the time step restriction (17) is a sufficient (but not necessary) condition to satisfy (18). Indeed, due to that $\left|\sum_j \Delta \text{up}^n_{i,\text{in},j}\right| \leq \sum_j \left|\Delta \text{up}^n_{i,\text{in},j}\right|$, a bigger Δt than in (17) could still be able to ensure the LED condition (18). Furthermore, it is emphasized that, within the framework of the implementation into the DEM/RDEM approach, the time step Δt is additionally restricted by acoustic wave speeds.

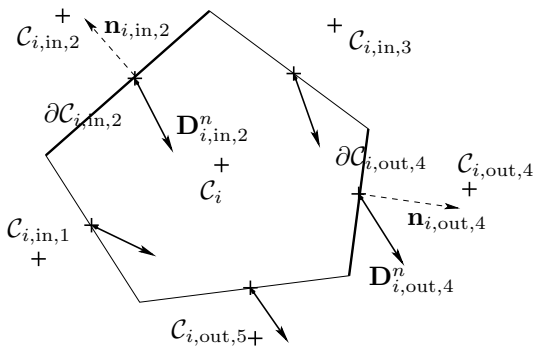

Figure 21: Two dimensional finite volume cell.

Using the first order upwind scheme, the contribution of the outlet boundary $\partial\mathcal{C}_{i,\text{out},j}$ to the neighboring cell $\mathcal{C}_{i,\text{out},j}$ is quantified by the exiting volume:

$$\Delta\text{up}^n_{i,\text{out},j} = \left(\alpha^n_i - \alpha^n_{i,\text{out},j}\right) |\partial\mathcal{C}_{i,\text{out},j}|\, \mathbf{D}^n_{i,\text{out},j} \cdot \mathbf{n}_{i,\text{out},j}\Delta t.$$

Following the idea introduced in Section 4, the high resolution scheme here designed for the multi-dimensional case is of the formulation,

$$\alpha^{n+1}_i = \alpha^n_i + \sum_j (1 - \lambda^n_{i,\text{in},j})\frac{\Delta\text{up}^n_{i,\text{in},j}}{|\mathcal{C}_i|} + \sum_j \lambda^n_{i,\text{out},j}\frac{\Delta\text{up}^n_{i,\text{out},j}}{|\mathcal{C}_i|}, \tag{19}$$

with $0 \le \lambda^n_{i,\text{in},j}, \lambda^n_{i,\text{out},j} \le 1$. (19) degenerates to the upwind scheme when setting $\lambda^n_{i,\text{in},j}, \lambda^n_{i,\text{out},j} = 0$ for all j. On the other hand, an unstable downwind scheme is recovered if putting $\lambda^n_{i,\text{in},j}, \lambda^n_{i,\text{out},j} = 1$ for all j. (19) can be understood as follows: among the volume Δup^n_j generated and transported across the boundary $\partial\mathcal{C}_{i,j}$ by the first order upwind method, a part of it (the percentage is λ^n_j) is returned back to its upwind cell. That is, based on the upwind result in $\mathcal{C}_i$, we return the amount of $\lambda^n_{i,\text{in},j}\Delta\text{up}^n_{i,\text{in},j}$ to its inlet neighbor $\mathcal{C}_{i,\text{in},j}$, and on the other side, fetch the amount of $\lambda^n_{i,\text{out},j}\Delta\text{up}^n_{i,\text{out},j}$ from its outlet neighbor $\mathcal{C}_{i,\text{out},j}$. Obviously, with bigger values of $\lambda^n_{i,\text{in},j}, \lambda^n_{i,\text{out},j}$, the scheme is more accurate. However, the local LED condition of (18) should always be verified.

Above all, as done in Section 4, a second order accurate scheme can be obtained by using the slope limiting strategy. In this framework, the value of $\lambda^n_{i,\text{out},j}$ is determined by

$$\lambda^n_{i,\text{out},j} = \frac{\alpha^n_i - \alpha^n_{\text{f,out},j}}{\alpha^n_i - \alpha^n_{i,\text{out},j}}, \text{ when } \alpha^n_i \ne \alpha^n_{i,\text{out},j}. \tag{20}$$

$\alpha^n_{\text{f,out},j}$ in (20) the reconstructed value at the boundary $\partial\mathcal{C}_{i,\text{out},j}$ within cell $\mathcal{C}_i$ using slope limiter. $\lambda^n_{i,\text{in},j}$ is determined in the same manner.

In the following we seek a higher accuracy of interface using algebraic techniques to (18) and (19). For simplicity, a unique value of percentage $\lambda^n_{i,\text{out}}$ is imposed for all outlet boundaries $\{\partial\mathcal{C}_{i,\text{out},j}\}$. That is,

$$\lambda^n_{i,\text{out},j} = \lambda^n_{i,\text{out}}, \text{ for any } j.$$

Thus, by defining $\Delta\text{up}^n_{i,\text{out}} = \sum_j \Delta\text{up}^n_{i,\text{out},j}$ for cell $\mathcal{C}_i$, (18) is rewritten as follows:

$$\alpha^n_i + \sum_j (1 - \lambda^n_{i,\text{in},j})\frac{\Delta\text{up}^n_{i,\text{in},j}}{|\mathcal{C}_i|} + \lambda^n_{i,\text{out}}\frac{\Delta\text{up}^n_{i,\text{out}}}{|\mathcal{C}_i|} \ge m^n_i, \tag{21}$$

$$\alpha^n_i + \sum_j (1 - \lambda^n_{i,\text{in},j})\frac{\Delta\text{up}^n_{i,\text{in},j}}{|\mathcal{C}_i|} + \lambda^n_{i,\text{out}}\frac{\Delta\text{up}^n_{i,\text{out}}}{|\mathcal{C}_i|} \le M^n_i. \tag{22}$$

It is easy to verify that, when putting $\lambda^n_{i,\text{out}} = 0$, both (21) and (22) are fulfilled for any value of $\lambda^n_{i,\text{in},j}$, by writing α^{n+1}_i in means of an average among α^n_i and that of its inlet neighbors $\{\alpha^n_{i,\text{in},j}\}$ as done in (16). This fact furthermore gives the following result: if $\Delta\text{up}^n_{i,\text{out}} < 0$, (22) is satisfied; on the other hand, if $\Delta\text{up}^n_{i,\text{out}} > 0$, (21) is satisfied. It follows the summary of restrictive conditions as below:

$$\begin{cases} 0 \le \lambda^n_{i,\text{out}} \le 1; \\ 0 \le \lambda^n_{i,\text{in},j} \le 1, \ \forall j; \\ \lambda^n_{i,\text{out}} \le \begin{cases} \dfrac{1}{\left|\Delta\text{up}^n_{i,\text{out}}\right|}\left[|\mathcal{C}_i|\,(\alpha^n_i - m^n_i) + \displaystyle\sum_j (1 - \lambda^n_{i,\text{in},j})\Delta\text{up}^n_{i,\text{in},j}\right], \text{ if } \Delta\text{up}^n_{i,\text{out}} < 0; \\ \dfrac{1}{\left|\Delta\text{up}^n_{i,\text{out}}\right|}\left[|\mathcal{C}_i|\,(M^n_i - \alpha^n_i) - \displaystyle\sum_j (1 - \lambda^n_{i,\text{in},j})\Delta\text{up}^n_{i,\text{in},j}\right], \text{ if } \Delta\text{up}^n_{i,\text{out}} > 0. \end{cases} \end{cases} \tag{23}$$

It is certain that the system of inequalities (23) has its solution $\{\lambda^n_{i,\text{out}}\}$ (for instance, $\lambda^n_{i,\text{out}} = 0$ is inside its solution region for any $\lambda^n_{i,\text{in},j}$). Unfortunately (23) involves almost all the intercell boundaries in the whole domain considered, which gives serious algebraic difficulties to find the full region of solution for $\lambda^n_{i,\text{out}}$. As

done for the one dimensional case in Section 4 (similar technique as in [4]), we use a sub-region of the solution of (23) as follows:

$$\left\{\begin{array}{l} 0 \leq \lambda^n_{i,\text{out}} \leq 1; \\ \lambda^n_{i,\text{out}} \leq \left\{\begin{array}{l} \dfrac{1}{|\Delta \text{up}^n_{i,\text{out}}|}\Big[|\mathcal{C}_i|\,(\alpha^n_i - m^n_i) + \displaystyle\sum_j \frac{1}{2}\Big(1 - \text{sign}(\Delta \text{up}^n_{i,\text{in},j})\Big)\Delta \text{up}^n_{i,\text{in},j}\Big], \text{ if } \Delta \text{up}^n_{i,\text{out}} < 0; \\ \dfrac{1}{|\Delta \text{up}^n_{i,\text{out}}|}\Big[|\mathcal{C}_i|\,(M^n_i - \alpha^n_i) - \displaystyle\sum_j \frac{1}{2}\Big(1 + \text{sign}(\Delta \text{up}^n_{i,\text{in},j})\Big)\Delta \text{up}^n_{i,\text{in},j}\Big], \text{ if } \Delta \text{up}^n_{i,\text{out}} > 0. \end{array}\right. \end{array}\right. \tag{24}$$

Hence, the optimized value of $\lambda^n_{i,\text{out}}$ can be determined locally.

References

[1] A Beccantini and E Studer. The reactive Riemann problem for thermally perfect gases at all combustion regimes. *International Journal for Numerical Methods in Fluids*, 64:269–313, 2010.

[2] Rémi Abgrall and Richard Saurel. Discrete equations for physical and numerical compressible multiphase mixtures. *Journal of Computational Physics*, 186:361–396, 2003.

[3] O Lemetayer, J Massoni, and R Saurel. Modelling evaporation fronts with reactive Riemann solvers. *Journal of Computational Physics*, 205:567–610, 2005.

[4] B Després and F Lagoutière. Contact Discontinuity Capturing Schemes for Linear Advection and Compressible Gas Dynamics. *Journal of Scientific Computing*, 16(4):479–524, 2002.

[5] Alberto Beccantini and Kunkun Tang. The Reactive Discrete Equations Method for the (reactive) Euler Equations: the minmod reconstruction versus the antidiffusive approach. Technical report, CEA Saclay DM2S/SFME/LTMF/RT/10-007/A, 2010.

[6] A.A. Efimenko and S.B. Dorofeev. CREBCOM code system for description of gaseous combustion. *Journal of Loss Prevention in the Process Industries*, 14(6):575–581, November 2001.

[7] S Kudriakov, F Dabbene, E Studer, a Beccantini, J Magnaud, H Paillere, a Bentaib, a Bleyer, J Malet, and E Porcheron. The TONUS CFD code for hydrogen risk analysis: Physical models, numerical schemes and validation matrix. *Nuclear Engineering and Design*, 238:551–565, June 2007.

[8] J. García, D. Baraldi, E. Gallego, A. Beccantini, A. Crespo, O.R. Hansen, S. Hø iset, A. Kotchourko, D. Makarov, and E. Migoya. An intercomparison exercise on the capabilities of CFD models to reproduce a large-scale hydrogen deflagration in open atmosphere. *International Journal of Hydrogen Energy*, 35(9):4435–4444, May 2010.

[9] S. Kokh and F. Lagoutiere. An anti-diffusive numerical scheme for the simulation of interfaces between compressible fluids by means of a five-equation model. *Journal of Computational Physics*, 229(8):2773–2809, April 2010.

[10] Jean-Marc Delhaye. Équations fondamentales des écoulements diphasiques. Technical report, Commissariat à l'énergie atomique, CEA-R-3429, 1968.

[11] Mamoru Ishii. *Thermo-fluid Dynamic Theory of Two-phase Flow*. Eyrolles, Paris, 1975.

[12] F Harlow and A Amsden. Fluid dynamics. Technical report, Los Alamos National Laboratory, LA-4700, 1971.

[13] Olivier Le Metayer. *Modélisation et résolution de la propagation de fronts perméables. Application aux fronts d'évaporation et de détonation*. PhD thesis, Aix Marseille 1, 2003.

[14] Donald A. Drew and Stephen L. Passman. *Theory of Multicomponent Fluids, Applied Mathematical Sciences, Vol. 135*. Springer, New York, 1998.

[15] Richard Saurel, Jacques Massoni, and François Renaud. A numerical method for one-dimensional compressible multiphase flows on moving meshes. *International Journal for Numerical Methods in Fluids*, 54:1425–1450, 2007.

[16] Alberto Beccantini, Pascal Galon, and Vincent Faucher. Numerical investigation of a mechanical device subjected to a deflagration-to-detonation transition. In *International Conference on Hydrogen Safety (ICHS)*, San Francisco, USA, 2011.

[17] A Murrone and H Guillard. A five equation reduced model for compressible two phase flow problems. *Journal of Computational Physics*, 202:664–698, 2005.
[18] Ali Zein, Maren Hantke, and Gerald Warnecke. Modeling phase transition for compressible two-phase flows applied to metastable liquids. *Journal of Computational Physics*, 229(8):2964–2998, April 2010.
[19] M. J. Ivings, D. M. Causon, and E. F. Toro. On Riemann solvers for compressible liquids. *International Journal for Numerical Methods in Fluids*, 28(3):395–418, September 1998.
[20] E. F. Toro. *Riemann Solvers and Numerical Methods for Fluid Dynamics: A Practical Introduction*. Springer-Verlag, first edition, 1997.
[21] R Abgrall. How to Prevent Pressure Oscillations in Multicomponent Flow Calculations: A Quasi Conservative Approach. *Journal of Computational Physics*, 125(1):150–160, April 1996.
[22] R Saurel and R Abgrall. A multiphase Godunov method for compressible multifluid and multiphase flows. *Journal of Computational Physics*, 150:425–467, 1999.
[23] Alberto Beccantini. *Upwind Splitting Schemes for Ideal Gases Mixtures with Temperature-Dependent Specific Heat Capacities*. PhD thesis, Université d'Evry, 2000.
[24] Antony Jameson. A perspective on computational algorithms for aerodynamic analysis and design. *Progress in Aerospace Sciences*, 37:197–243, 2001.
[25] F Petitpas, E Franquet, R Saurel, and O Lemetayer. A relaxation-projection method for compressible flows. Part II: Artificial heat exchanges for multiphase shocks. *Journal of Computational Physics*, 225(2):2214–2248, August 2007.
[26] D.R. Stull and H. Prophet. *JANAF thermochemical tables*. U.S. Dept. of Commerce, National Bureau of Standards, Washington, D.C., second edition, 1971.
[27] James J Quirk and Smadar Karni. On the dynamics of a shock-bubble interaction. *Journal of Fluid Mechanics*, 318:129–163, 1996.
[28] K M Shyue. A wave-propagation based volume tracking method for compressible multicomponent flow in two space dimensions. *Journal of Computational Physics*, 215:219–244, 2006.
[29] J.-F. Haas and B. Sturtevant. Interaction of weak shock waves with cylindrical and spherical gas inhomogeneities. *Journal of Fluid Mechanics*, 181:41–76, 1987.
[30] A.L. Kuhl, M.M. Kamel, and A.K. Oppenheim. Pressure waves generated by steady flames. *Symposium (International) on Combustion*, 14(1):1201 – 1215, 1973.